Journal of Sol-Gel Science and Technology (2026) 118:53
https://doi.org/10.1007/s10971-026-07184-2

ORIGINAL PAPER

Hierarchical nanoconfinement in a green chitosan-copper oxide nanocomposite decouples cytotoxicity from pro-healing bioactivity

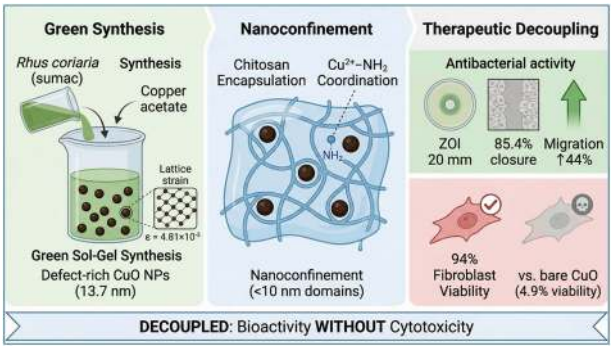
Aml Mahmoud Mohammed[1] · A. M. Ahmed[1] · H. F. Mohamed[1] · Walaa M. Abd El-Raheem[2] · Alaa Hassan Said[3]

Received: 4 April 2026 / Accepted: 28 April 2026 / Published online: 20 May 2026
© The Author(s) 2026

Abstract

The therapeutic use of copper oxide nanoparticles for wound healing is limited by intrinsic cytotoxicity arising from uncontrolled Cu^{2+} release. This study reports a hierarchical nanocomposite design that decouples bioactivity from cytotoxicity via green sol–gel synthesis followed by polymer-mediated nanoconfinement. Green synthesis using *Rhus coriaria* (sumac) extract contributed to structural changes through two primary mechanisms: (i) phytochemicals adsorbed to growing crystal surfaces, limiting Ostwald ripening and restricting crystallite growth; (ii) incorporation of organic capping agents induced lattice distortions during nucleation. Williamson-Hall analysis revealed a 54% reduction in crystallite size (to 13.7 nm) and an 89% increase in lattice microstrain ($\varepsilon = 4.81 \times 10^{-3}$) compared to conventionally synthesized CuO NPs. These green-synthesized CuO NPs were encapsulated within a chitosan matrix via coordination chemistry. X-ray diffraction showed severe attenuation of CuO Bragg peaks, confirming nanoconfinement of crystalline domains below 5 nm. Fourier-transform infrared spectroscopy revealed a hypsochromic shift of the amide I band from 1653 cm^{-1} to 1567 cm^{-1}, evidencing interfacial Cu^{2+}–NH_2coordination. At 125 µg/mL, the nanocomposite maintained 94.0% viability in human dermal fibroblasts versus 4.9% for bare CuO NPs, while enhancing fibroblast migration by 44% and achieving 85.4% in vitro wound closure over 48 h. The nanocomposite also exhibited broad-spectrum antibacterial activity (inhibition zones up to 20 mm), comparable to gentamicin. This work demonstrates that green sol–gel synthesis combined with polymer nanoconfinement produces a hierarchical chitosan-CuO hybrid that balances safety and efficacy, offering a generalizable design strategy for metal-oxide nanotherapeutics.

Graphical Abstract



Keywords Sol–gel synthesis · Green synthesis · Chitosan · Copper oxide · Nanocomposite · Wound healing

✉ Alaa Hassan Said
alaa.elkareem@sci.svu.edu.eg

[1] Physics Department, Faculty of Science, Sohag University, Sohag, Egypt

[2] Botany and Microbiology Department, Faculty of Science, Sohag University, Sohag, Egypt

[3] Electronics and Nano Devices Lab, Faculty of Science, Qena University, Qena, Egypt

Highlights

- Green sol–gel synthesis creates defect-rich CuO cores (13.7 nm, high strain).
- Chitosan encapsulation enables nanoconfinement and Cu^{2+}–NH_2 coordination.
- Nanocomposite decouples bioactivity from cytotoxicity (94% vs. 4.9% viability).
- Enhanced wound closure (85.4%) and fibroblast migration (44% increase).
- Broad-spectrum antibacterial activity matches or exceeds gentamicin.

1 Introduction

Chronic and non-healing wounds, such as diabetic ulcers, pressure sores, and burn injuries, represent a growing global healthcare challenge. They affect millions of patients annually, imposing severe personal burdens and high economic costs on healthcare systems worldwide [1, 2]. In developed nations, chronic wounds impact approximately 2% of the population, with annual management costs in the United States alone estimated between $28 and $31 billion [3]. The complex pathophysiology of impaired healing involves persistent inflammation, microbial infection, dysregulated angiogenesis, and reduced fibroblast proliferation and migration. Key obstacles include the formation of bacterial biofilms and a hyperinflammatory microenvironment that stalls the transition from the inflammatory to the proliferative phase of healing [4, 5]. Conventional wound care strategies are frequently inadequate, underscoring an urgent need for advanced therapeutic platforms capable of simultaneously promoting tissue regeneration, preventing infection, and modulating the wound microenvironment [6].

Metal oxide nanoparticles (MONPs) have emerged as promising candidates for advanced wound management due to their tunable physicochemical properties and multifaceted biological activities [7, 8]. Among these, copper oxide nanoparticles (CuO NPs) are particularly compelling for their potent intrinsic antimicrobial activity, ability to stimulate angiogenesis, and role as essential cofactors in enzymes critical for extracellular matrix formation, such as lysyl oxidase [9]. However, the clinical translation of CuO NPs is severely hampered by their well-documented cytotoxicity, primarily driven by the rapid release of Cu^{2+} ions, uncontrolled generation of reactive oxygen species (ROS), and subsequent induction of oxidative stress and mitochondrial dysfunction in mammalian cells [10, 11]. This fundamental conflict between therapeutic potential and inherent toxicity highlights the critical need for innovative nanomaterial design strategies that can mitigate adverse effects while preserving or enhancing desired bioactivity.

Green synthesis of NPs using plant extracts has gained prominence as a sustainable alternative to conventional chemical methods. This approach offers distinct advantages, including reduced environmental impact, enhanced biocompatibility, and formation of a stabilizing phytochemical corona that can impart additional antioxidant and anti-inflammatory properties [12–14]. *Rhus coriaria* (sumac), rich in polyphenols, flavonoids, and organic acids, serves as an effective reducing and capping agent, while its phytoconstituents may contribute beneficial bioactivities relevant to wound healing [15]. Recent studies have demonstrated the antimicrobial potential of phytochemicals and their synthesized nanomaterials against various pathogens [16–20].

To further enhance biocompatibility, biopolymers such as chitosan are widely employed for NP coating and encapsulation. Chitosan, a cationic polysaccharide derived from chitin, is FDA-approved for wound care owing to its biodegradability, mucoadhesiveness, hemostatic properties, and inherent antimicrobial activity [21]. As a coating material, chitosan can effectively modulate metal ion release kinetics, attenuate ROS generation, improve colloidal stability, and enhance cellular uptake—thereby potentially widening the therapeutic window of MONPs [22].

Therefore, this study aims to develop, characterize, and evaluate a novel multifunctional wound-healing nanoplatform. We synthesized CuO NPs via both chemical and biogenic routes using *Rhus coriaria* extract, followed by chitosan encapsulation to form a chitosan-CuO nanocomposite. We hypothesized that this hierarchical design, integrating defect engineering through green synthesis with polymer-mediated nanoconfinement, would fundamentally decouple the beneficial wound-healing properties of CuO NPs from their toxicological liabilities.

2 Materials and methods

This work was approved by the Ethics Committee of Sohag University, Faculty of Science. All procedures were conducted in accordance with the relevant institutional guidelines and regulations. No human or animal subjects were involved in this study.

2.1 Materials

Copper(II) acetate monohydrate ($Cu(CH_3COO)_2{\cdot}H_2O$, ≥98%) and sodium hydroxide (NaOH, ≥97%) were purchased from Sigma-Aldrich (USA). Low molecular weight chitosan (deacetylation degree ≥75%) and glacial acetic acid were obtained from Merck (Germany). Dried *Rhus coriaria*

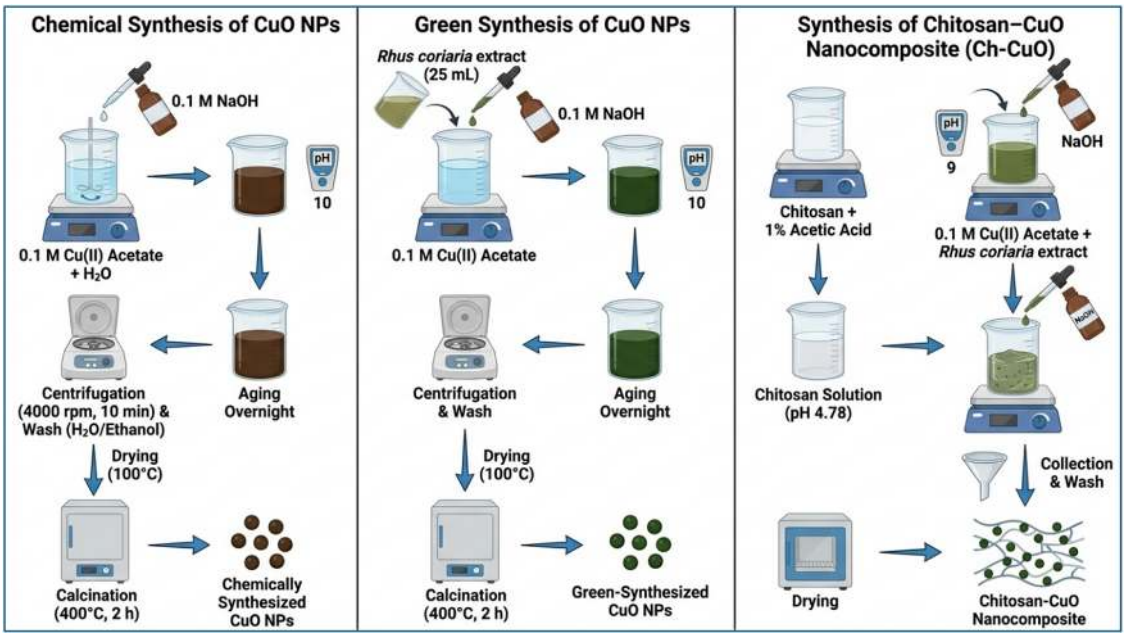


Fig. 1 Schematic overview of the synthesis of chemical and green chitosan CuO NPs

fruits were procured from a local herbal market in Sohag, Egypt. Dimethyl sulfoxide (DMSO) and ethanol were of analytical grade. The MTT assay kit (Cat. No. M6494) and Dulbecco's Modified Eagle Medium (DMEM) supplemented with 10% fetal bovine serum (FBS) and 1% penicillin–streptomycin were sourced from Thermo Fisher Scientific (USA). Bacterial strains, including methicillin-resistant *Staphylococcus aureus* (MRSA, ATCC 43300), *Streptococcus pyogenes* (ATCC 19615), *Klebsiella pneumoniae* (ATCC 700603), and *Escherichia coli* (ATCC 25922), were acquired from ATCC. Human foreskin fibroblast cells (HFB4) were provided by the Cell Culture Unit, Faculty of Science, Sohag University.

2.2 Preparation of *Rhus coriaria* (Sumac) extract

Dried *Rhus coriaria* seeds were washed thoroughly with distilled water, air-dried at room temperature, and ground into fine powder. A total of 50 g of powdered seeds was added to 200 mL distilled water and heated under magnetic stirring until boiling. The mixture was maintained at boiling temperature for 40 min, then filtered through Whatman No. 1 filter paper. The resulting aqueous extract was stored at 4 °C for subsequent use [23].

2.3 Synthesis of copper oxide nanoparticles

2.3.1 Chemical synthesis of CuO NPs

A 0.1 M aqueous solution of copper(II) acetate monohydrate was prepared in 50 mL distilled water and stirred vigorously. A 0.1 M NaOH solution was added dropwise to adjust the pH to 10, resulting in a color change from light blue to dark brown. The mixture was aged overnight at room temperature [24]. The precipitate was collected via centrifugation at 4000 rpm for 10 min, washed repeatedly with distilled water and ethanol, dried at 100 °C, and calcined at 400 °C for 2 h to obtain chemically synthesized CuO NPs (Fig. 1).

2.3.2 Green synthesis of CuO NPs

To 50 mL of 0.1 M copper(II) acetate solution, 25 mL of *Rhus coriaria* extract was added dropwise under continuous stirring. The pH was adjusted to 10 using 0.1 M NaOH, inducing a color change from light blue to dark green [23]. The mixture was aged overnight, washed, centrifuged, dried at 100 °C, and calcined at 400 °C for 2 h to produce green-synthesized CuO NPs (Fig. 1).

2.4 Synthesis of chitosan–CuO nanocomposite (Ch-CuO)

A 1% (w/v) chitosan solution was prepared by dissolving chitosan in 1% (v/v) acetic acid under continuous stirring for 24 h. The pH was adjusted to 4.78 using 0.1 M NaOH. For nanocomposite formation, 20 mL of *Rhus coriaria* extract was added dropwise to 0.1 M copper(II) acetate solution, stirred for 1 h, and pH adjusted to 9 with NaOH. Subsequently, 20 mL of chitosan solution was added dropwise under stirring for 2 h, resulting in a gel-like complex [25]. The product was collected, washed, and dried for further characterization (Fig. 1).

2.5 Characterization of nanoparticles

The crystalline structure of the chemically synthesized CuO NPs, green-synthesized CuO NPs, and Chitosan CuO nanocomposite was analyzed using an X-ray diffractometer (D8 Advance with DAVINCI design, Bruker, Germany). Measurements were performed using Cu Kα radiation ($\lambda = 1.5418$ Å) at an operating voltage of 40 kV and a current of 40 mA. Crystallite sizes were calculated using the Debye–Scherrer equation [12].

$$D = \frac{K\lambda}{FWHM\ \cos\ \theta}$$

where K is the Scherrer constant (0.89) for spherical particles, λ is the X-ray wavelength (1.5406 Å), FWHM is the full width at half maximum in radians after instrumental broadening correction, and θ is the Bragg angle.

To separate the contributions of crystallite size and lattice strain to peak broadening, Williamson-Hall analysis was performed. The relationship [26]:

$$FWHM\cos\theta = \frac{K\lambda}{D} + 4\varepsilon\ \sin\ \theta$$

was applied, where ε represents the microstrain. Linear regression of FWHM cosθ versus 4sinθ plots for five characteristic peaks—(110), (–111), (111), (–202), and (020)—yielded the slope (ε) and y-intercept (related to D). The dislocation density (δ) was subsequently calculated using [26]:

$$\delta = \frac{1}{D^2}\text{or alternatively}\delta = \frac{\varepsilon^2}{b^2}$$

where b is the Burgers vector (2.6 Å for monoclinic CuO).

Fourier-transform infrared spectroscopy (FTIR) was performed using a Bruker spectrometer equipped with a Platinum-ATR module to identify functional groups present in the NPs and nanocomposite. UV-visible absorption spectra were recorded using a Jenway 7305 spectrophotometer to confirm NPs formation. High-resolution transmission electron microscopy (HR-TEM) was conducted using a JEOL JEM-2100 microscope operating at 200 kV to examine particle morphology, size, and distribution.

2.6 Antibacterial activity assay

The antibacterial activity of chemically synthesized CuO NPs, green-synthesized CuO NPs, and chitosan green CuO nanocomposite was evaluated using the standard agar well diffusion method [27]. The assay was performed against a panel of clinically relevant Gram-positive and Gram-negative pathogens [28], including Methicillin-resistant *Staphylococcus aureus* (MRSA, ATCC 43300), *Streptococcus pyogenes* (ATCC 19615), *Klebsiella pneumoniae* (ATCC 700603), and *Escherichia coli* (ATCC 25922). All strains were obtained from the Department of Medical Microbiology & Immunology, Faculty of Medicine, Sohag University, and were identified by standard morphological and biochemical tests.

For the assay, a single colony of each strain was inoculated into 10 mL of sterile nutrient broth and incubated at 37 °C for 24 h under continuous shaking at 120 rpm. The optical density of each broth culture was standardized to a 0.5 McFarland turbidity (approximately 1.5×10^8 CFU·mL^{-1}) using sterile saline, in accordance with established guidelines for antimicrobial susceptibility testing. A volume of 100 µL of each standardized suspension was then spread uniformly onto the surface of nutrient agar plates using a sterile swab. Wells of 6 mm diameter were punched into the inoculated agar.

Each well was loaded with 100 µL of the corresponding test suspension. The test samples (CuO NPs, green CuO NPs, and green chitosan CuO nanocomposite) were tested at a concentration of 500 µg/mL (dispersed in dimethyl sulfoxide, DMSO). Pure DMSO served as the negative control, and gentamicin (10 µg per well) was used as the positive antibiotic control. All plates were incubated at 37 °C for 24 h. After incubation, the antibacterial activity was quantified by measuring the diameter of the clear zones of inhibition (ZOI) in millimeters using a digital caliper.

2.7 Cytotoxicity assay (MTT)

Cytotoxicity was evaluated using the MTT (3-(4,5-dimethylthiazol-2-yl)-2,5-diphenyltetrazolium bromide) viability assay [14]. Human foreskin fibroblast cells (HFB4) were seeded in 96-well plates at a density of 1×10^4 cells per well in 100 µL of complete Dulbecco's Modified Eagle Medium (DMEM) supplemented with 10% fetal bovine serum (FBS) and 1% penicillin/streptomycin, then incubated at 37 °C under 5% $CO_2$for 24 h to achieve ~80% confluence. Following adhesion, the medium was aspirated, and the monolayer was gently rinsed twice with pre-warmed phosphate-buffered saline (PBS). Serial dilutions of test samples (CuO NPs, green CuO NPs, and green chitosan-CuO nanocomposite) ranging from 31.25 to 1000 µg/mL were prepared in DMEM, and 100 µL of each concentration was added to triplicate wells. Wells containing maintenance medium alone served as untreated controls. After 24 h treatment, 20 µL of MTT solution (5 mg/mL in PBS) was added to each well. Plates were gently agitated on an orbital shaker (150 rpm, 5 min) and incubated for 4 h at 37 °C to allow viable cells to metabolize MTT into insoluble formazan crystals. Following incubation, the medium was carefully removed without disturbing the crystals, and the

formazan product was solubilized by adding 200 µL of DMSO per well, followed by agitation (150 rpm, 5 min). Absorbance was measured at 560 nm with a reference filter at 620 nm using a microplate reader. Cell viability was expressed as a percentage relative to the untreated control, calculated according to the equation [12]:

$$\text{Cell Viability}(\%) = \left(\frac{A_{sample} - A_{\text{blank}}}{A_{\text{control}} - A_{\text{blank}}}\right) \times 100$$

where A_{sample}, A_{control}, and A_{blank} represent the absorbance of treated wells, untreated control wells, and cell-free medium blanks, respectively.

Cell morphology was assessed in parallel using an inverted phase-contrast microscope, where monolayers were examined for hallmark features of cytotoxicity, including cell rounding, detachment, shrinkage, cytoplasmic granulation, cellular and nuclear swelling, membrane rupture, chromatin flocculation, cell shrinkage, membrane blebbing, nuclear condensation (pyknosis) and fragmentation (karyorrhexis). Representative images were captured for documentation, and morphological changes were scored qualitatively.

2.8 Scratch wound healing assay

HFB4 cells were seeded in 6-well plates and grown to confluence. A uniform scratch was created using a sterile 200 µL pipette tip. After washing with PBS, fresh medium containing NPs (125 µg/mL) was added. Images were captured at 0 and 48 h using an Olympus CKX53 inverted microscope. Wound width and area were measured using ImageJ software. Migration rate (RM) and wound closure percentage were calculated as [29]

$$\text{RM}\,(\mu\text{m/h}) = \frac{\text{Wt} - \text{W}_\text{f}}{\text{t}}$$

$$\text{Wound Closure}(\%) = \left(\frac{A_0 - A_t}{A_0}\right) \times 100$$

where W_i and W_f are initial and final wound widths, A_0 and A_t are wound areas at time 0 and t, and t is time in hours.

2.9 Statistical analysis

All experiments were performed with a minimum of three independent biological replicates, each comprising three technical replicates ($n = 3$). Data are presented as mean ± standard deviation (SD). Statistical analysis was performed using IBM SPSS Statistics (Version 26.0, Armonk, NY, USA). For comparisons among multiple groups, one-way analysis of variance (ANOVA) was applied, followed by Tukey's honestly significant difference (HSD) post-hoc test for pairwise comparisons when ANOVA indicated significant differences ($p < 0.05$). The normality of data distribution and homogeneity of variances were verified using Shapiro-Wilk and Levene's tests, respectively. For direct comparisons between two groups, Student's t test (two-tailed) was employed. A p-value < 0.05 was considered statistically significant, with the following notation used in figures: $^*p < 0.05$, $^{**}p < 0.01$, $^{***}p < 0.001$.

3 Results and discussion

3.1 Structural and crystallographic analysis via X-ray diffraction

X-ray diffraction (XRD) analysis was employed to systematically investigate the crystallographic evolution from conventional inorganic NPs to an engineered organic-inorganic hybrid nanocomposite. The comparative patterns of all synthesized materials (chemically synthesized CuO NPs, green-synthesized CuO NPs, pure chitosan, and the green chitosan-CuO nanocomposite) are presented in Fig. 2.

All copper oxide-containing samples exhibited diffraction patterns characteristic of the monoclinic tenorite phase (space group *C2/c*, ICDD 00-048-1548) [30, 31]. Distinct reflections at 2θ values corresponding to the (110), ($\bar{1}$11), (111), ($\bar{2}$02), (020), (202), ($\bar{1}$13), ($\bar{3}$11), and (220) crystallographic planes confirmed phase purity without detectable secondary phases or impurities (Fig. 2a). The sharp, well-defined peaks in CuO NPs indicated high crystallinity and well-developed crystalline domains, while the pattern of pure chitosan NPs (Fig. 2c) displayed the expected broad amorphous halo centered near 20°, characteristic of its semicrystalline polysaccharide structure [32].

A direct comparison between CuO NPs and green CuO NPs revealed significant structural alterations induced by the plant-mediated synthesis route. While both samples maintained identical peak positions, confirming preserved lattice parameters, the green CuO NP pattern exhibited pronounced peak broadening across all reflections. FWHM of the dominant ($\bar{1}$11) peak increased from 0.24° in CuO NPs to 0.52° in green CuO NPs, corresponding to a crystallite size reduction from 29.8 ± 1.5 nm to 13.7 ± 0.8 nm as calculated via the Scherrer equation. This 54% size reduction is attributed to phytochemical capping agents from *Rhus coriaria* extract that adsorb to growing crystal surfaces, limiting Ostwald ripening and promoting the formation of smaller, more uniform NPs [33].

Williamson-Hall analysis provided quantitative insight into the microstructural changes by decoupling size and strain contributions to peak broadening. Linear regression of FWHM·cosθ versus 4sinθ plots yielded excellent fits with R^2 values of 0.986 for CuO NPs and 0.992 for green

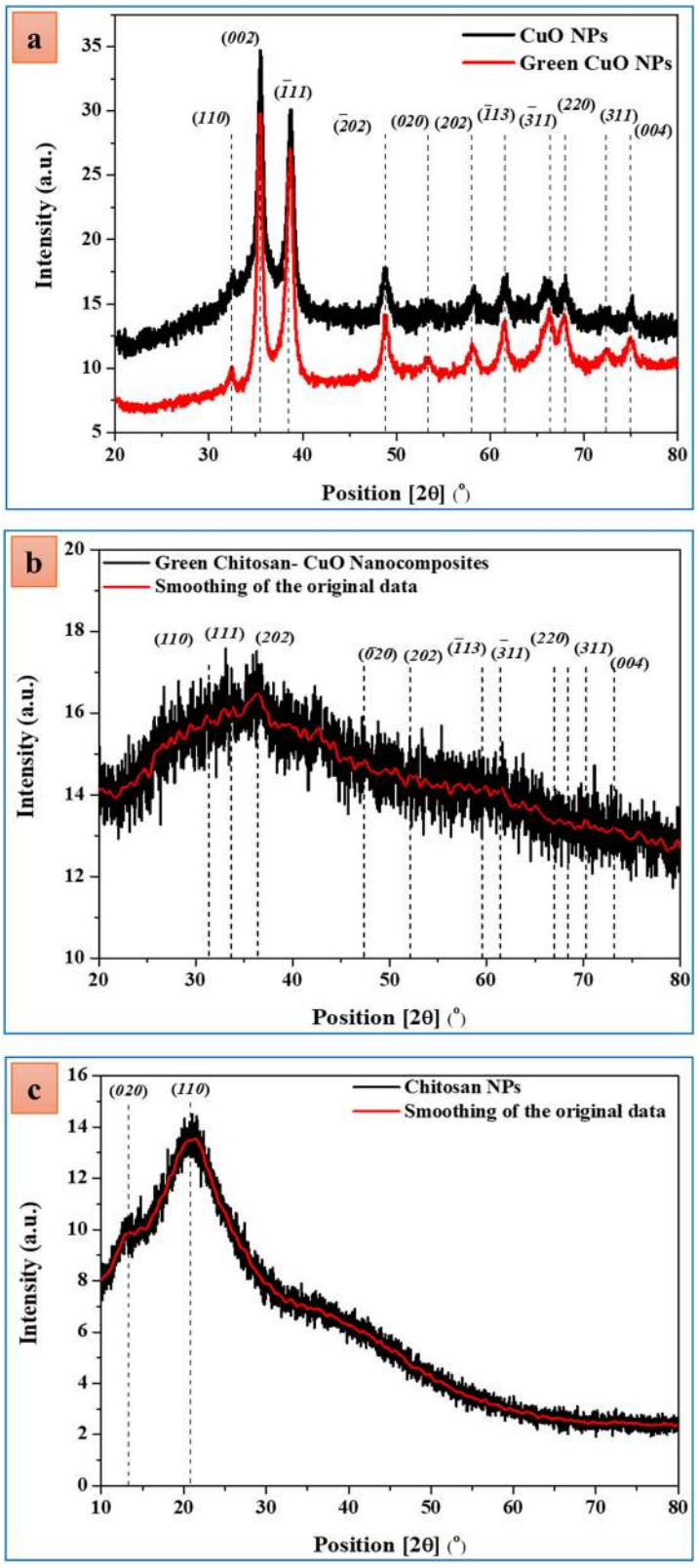


Fig. 2 X-ray diffraction patterns of synthesized nanomaterials. **a** Comparative plot of chemically synthesized and green-synthesized CuO NPs. **b** Pattern of green chitosan-CuO nanocomposite. **c** Pattern of pure chitosan NPs. Reference lines indicate monoclinic CuO phase (ICDD 00-048-1548)

CuO NPs (Supplementary Fig. S1). The analysis revealed microstrain values of $\varepsilon = 2.54 \times 10^{-3}$ for CuO NPs and $\varepsilon = 4.81 \times 10^{-3}$ for green CuO NPs, representing an 89% increase in lattice distortion through green synthesis (Supplementary Table S1). Correspondingly, the dislocation density increased from $0.77 \times 10^{15}\,m^{-2}$ to $2.83 \times 10^{15}\,m^{-2}$.

These findings demonstrate that green synthesis engineers a "defect-rich" crystalline state with controlled lattice imperfections that modulate surface reactivity [34, 35].

The XRD pattern of the green chitosan-CuO nanocomposite (Fig. 2b) exhibited a transformative architecture. The sharp Bragg peaks characteristic of crystalline copper oxide were severely attenuated, appearing only as faint, broad features superimposed on a dominant amorphous background. This near-complete suppression of crystalline signals indicates nanoconfinement of copper oxide domains within the chitosan matrix at dimensions below 5 nm, smaller than the X-ray coherence length. Concurrently, the chitosan amorphous halo broadened and shifted to approximately 21.5°, indicating decreased d-spacing likely resulting from ionic cross-linking between Cu^{2+} ions and chitosan amine groups [36, 37]. This structural configuration confirms successful encapsulation and suggests strong interfacial interactions that alter both polymer chain packing and inorganic domain morphology.

XRD analysis delineates a definitive structural progression across the synthesis strategies. Conventional chemical synthesis yields large, low-defect crystals with high crystallinity [38], whereas green synthesis produces smaller NPs with intentionally engineered lattice defects and increased microstrain [39]. The chitosan encapsulation step culminates in a hierarchical nanocomposite, where these ultrafine, strain-tuned crystalline domains are spatially confined within a responsive biopolymer matrix. This multi-scale architecture, spanning from atomic-scale lattice defects to nanoscale biopolymer confinement, establishes a material design optimized for controlled interfacial interactions. Critically, the increased microstrain and reduced crystallite size intrinsic to the green-synthesized cores enhance surface energy and reactivity, while the chitosan matrix governs the diffusion-limited release of bioactive species. This synergistic physicochemical foundation, combining a reactive nanocore with a rate-controlling biopolymer shell, directly establishes the material's multifunctional biological profile, reconciling potent antimicrobial activity with pro-regenerative cellular responses.

3.1.1 Morphological and nano-structural analysis via transmission electron microscopy

High-resolution transmission electron microscopy (HR-TEM) analysis of CuO NPs confirmed their nanoscale dimensions and agglomerative morphology. The micrograph showed nearly spherical particles with diameters of 9–17 nm, densely clustered into larger aggregates (Fig. 3a). Such agglomeration is characteristic of chemically synthesized metal oxides and is attributed to dominant van der Waals interactions and high surface energy [40, 41]. High-resolution imaging revealed well-defined lattice fringes with an interplanar spacing of 0.248 nm, corresponding to the $(1\bar{1}1)$ plane of monoclinic CuO (Fig. 3a inset), confirming the high crystallinity inferred from XRD. This agglomerated state is a key determinant of surface behavior and bioavailability [42].

In striking contrast, the green CuO NPs present a markedly different morphology. The particles are larger and more heterogeneous in size, with diameters ranging from 19 to 27 nm, and show a significantly reduced tendency to agglomerate (Fig. 3b). The particles appear more dispersed, often with irregular or quasi-spherical shapes and slightly diffused edges. This morphology is a direct consequence of the *Rhus coriaria* phytochemicals acting as in situ capping and growth-modulating agents. The organic matrix surrounding the nascent NPs during synthesis performs a dual function: it sterically limits particle–particle interaction—reducing agglomeration—while also modulating the kinetics of crystal growth, leading to larger, less uniform sizes and shapes [43]. The observed lower particle-to-particle contrast and diffuse boundaries are visual hallmarks of the lower crystallinity and potential surface-bound organic layer inferred from the broadened XRD peaks [44, 45]. Lattice fringes remain visible at 0.248 nm, indicating retained crystallinity despite surface modification. This confirms that the green synthesis route trades off the uniformity and high crystallinity of the chemical method for improved colloidal stability and a bio-organic interface.

The micrograph of the green chitosan–CuO nanocomposite confirms the successful architectural integration predicted by XRD (Fig. 3c). The image is dominated by a light, amorphous background corresponding to the chitosan matrix. Embedded within this matrix are darker, high-contrast spots with diameters predominantly below 10 nm, which are identified as the encapsulated CuO NPs. Their appearance as discrete, well-separated spots, rather than the dense agglomerates seen in CuO NPs, provides direct visual evidence of successful nanoconfinement within the polymer network. Chitosan effectively isolates the inorganic particles, preventing their aggregation. Furthermore, the spots appear slightly diffuse and integrated with the background, suggesting a strong interfacial interaction, likely through coordination between the copper ions and the amine ($–NH_2$) and hydroxyl (–OH) functional groups of chitosan. This encapsulation results in an extreme reduction in NP size within the composite, as the confined growth environment and polymer interactions limit crystal domain expansion. This visual evidence perfectly explains the XRD pattern of the nanocomposite, where the sharp Bragg peaks are replaced by an amorphous halo and extremely weak, broad residual scattering from these ultrafine, isolated crystalline domains [25, 46].

Pure chitosan NPs exhibit a featureless, amorphous morphology without discernible lattice structure (Fig. 3d), consistent with their semicrystalline polymer nature.

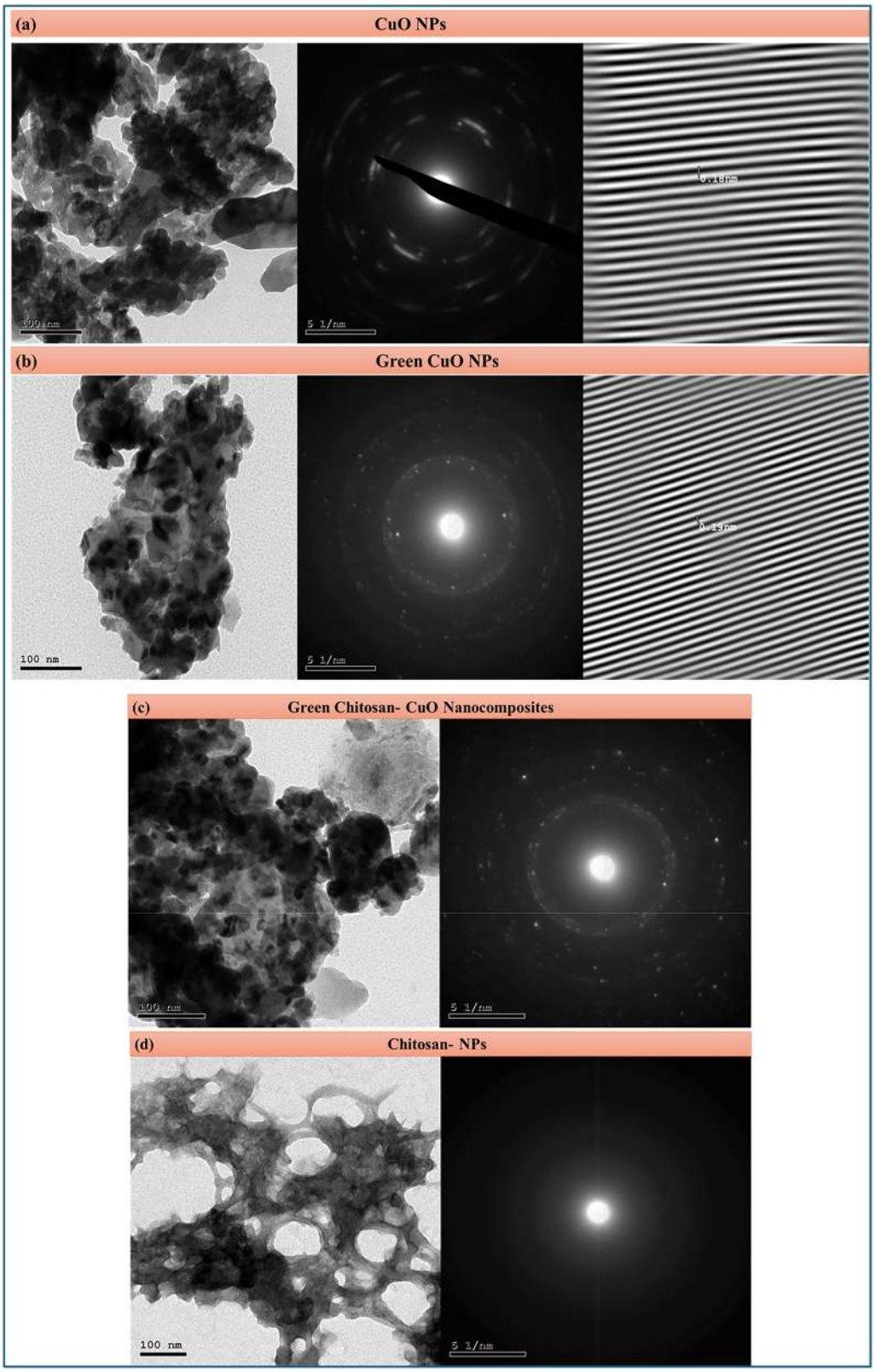


Fig. 3 TEM micrographs of **a** CuO NPs, **b** green CuO NPs, **c** chitosan–CuO nanocomposite, and **d** pure chitosan NPs. Scale bars: 100 nm. Insets in (**a**) and **b** show lattice fringes (0.248 nm spacing)

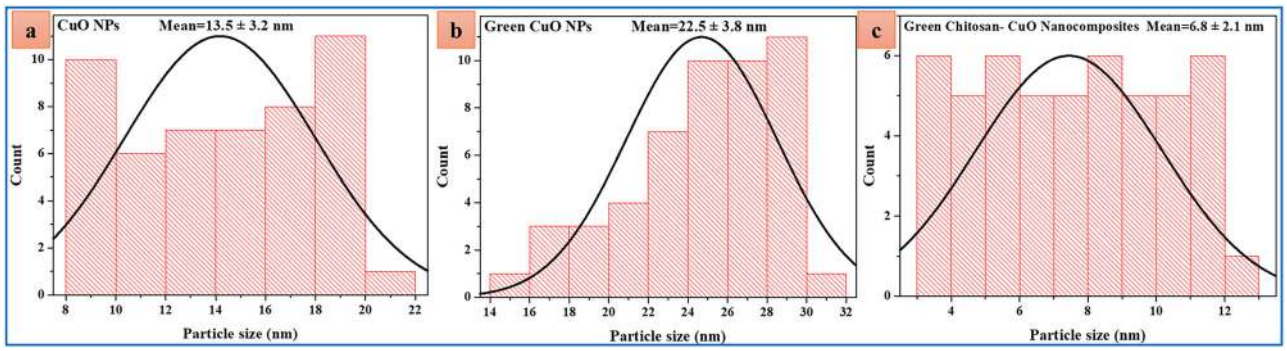


Fig. 4 Particle size distribution histograms derived from TEM analysis. **a** Chemically synthesized CuO NPs, **b** green-synthesized CuO NPs, and **c** CuO domains within the chitosan nanocomposite. Gaussian fits (black curves) show mean diameters of 13.5 ± 3.2 nm, 22.5 ± 3.8 nm, and 6.8 ± 2.1 nm, respectively. A summary of morphological and size characteristics is provided in Supplementary Table S2

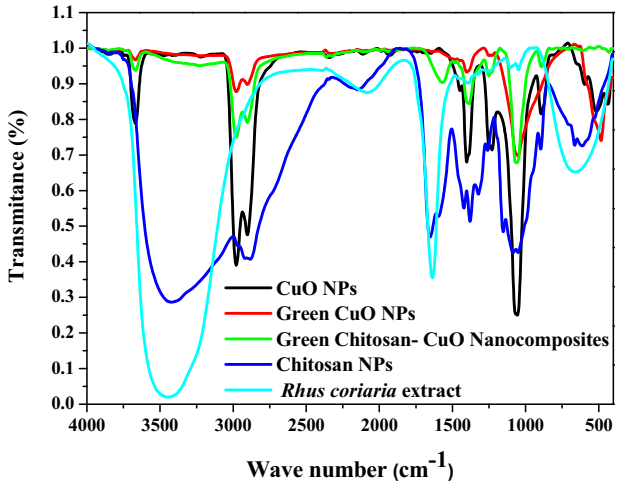


Fig. 5 FTIR spectra of *Rhus coriaria* aqueous extract, chemically synthesized CuO NPs, green-synthesized CuO NPs, pure chitosan, and the green chitosan-CuO nanocomposite

Quantitative particle size distributions derived from TEM micrographs (Fig. 4) further elucidate the synthesis-dependent size modulation. Chemically synthesized CuO NPs exhibited a mean diameter of 13.5 ± 3.2 nm with a right-skewed distribution (range: 8–20 nm). Green-synthesized CuO NPs were significantly larger (22.5 ± 3.8 nm, range: 15–30 nm) with a more symmetric distribution. Most notably, CuO domains within the chitosan nanocomposite were substantially smaller (6.8 ± 2.1 nm, range: 3–12 nm), confirming effective size confinement by the polymer matrix.

The TEM analysis thus completes the structural narrative: chemical synthesis produces small, crystalline, but highly agglomerated NPs; green synthesis yields larger, less crystalline, but better-stabilized particles via phytochemical capping; and chitosan encapsulation transforms them into a nanocomposite where ultrafine inorganic domains are isolated and stabilized within a continuous, biocompatible organic matrix. This progression from agglomerated crystals to organically-capped particles and finally to a polymer-nanoconfined hybrid is a critical determinant of how each material will interact with biological systems, influencing factors such as colloidal stability in physiological media, cellular uptake mechanisms, and the spatiotemporal release profile of bioactive copper ions.

3.1.2 Chemical composition and functional group analysis via Fourier-transform infrared spectroscopy

Fourier-transform infrared (FTIR) spectroscopy elucidates the chemical composition and interfacial interactions governing the synthesis and stability of nanomaterials. The spectra (Fig. 5) confirm the presence of phytochemical capping agents, verify the formation of copper oxide, and reveal the specific chemical interactions within the chitosan-copper oxide nanocomposite. A complete assignment of key FTIR absorption bands is provided in Supplementary Table S3.

The spectrum of the *Rhus coriaria* aqueous extract exhibits characteristic bands of polyphenols and flavonoids. A broad absorption band spanning 3200–3600 cm^{-1} corresponds to O–H stretching vibrations from water, phenolic acids (including gallic acid), and flavonoid hydroxyl groups [47, 48]. A strong band in the region 1600–1500 cm^{-1} is assigned to aromatic C=C stretching, confirming the presence of aromatic rings in polyphenolic compounds [49]. Additional bands between 600–900 cm^{-1} are attributed to aromatic C–H bending modes. These functional groups are integral to the reducing and capping capability of the extract [50].

The spectrum of pure chitosan shows its characteristic polysaccharide fingerprint. A broad band centered near 3420 cm^{-1} arises from the overlapping O–H and N–H stretching vibrations. The weak bands at approximately 2880 cm^{-1} are due to C–H stretching. A distinct peak at

1650 cm^{-1} is assigned to the C=O stretching of the amide I group (from residual N-acetylation), while the strong band at 1085 cm^{-1} corresponds to C–O–C stretching in the glucosamine backbone. The band between 890–900 cm^{-1} is characteristic of the chitosan polysaccharide structure [51].

The FTIR spectra of both chemically synthesized and green-synthesized CuO NPs confirm the formation of the metal oxide. A defining low-frequency band in the range 500–610 cm^{-1} is observed in all three inorganic-containing samples (CuO, green CuO and Chitosan green CuO nanocomposite). This band is characteristic of the Cu–O stretching vibration in the tenorite crystal structure, confirming successful oxide formation [52, 53].

Critical differences between the two synthesis routes are evident. The spectrum of chemically synthesized CuO NPs shows a relatively simple profile. A sharp O–H stretching band near 3670 cm^{-1} suggests the presence of adsorbed water or surface hydroxyls. The primary feature is the strong Cu–O band at ~513 cm^{-1} [54, 55].

In contrast, the spectrum of green CuO NPs is more complex, superimposing the inorganic signature with organic bands from the capping agents. In addition to the Cu–O band (shifted to ~500 cm^{-1}), it displays a broad O–H band (~ 3670 cm^{-1}), alkyl C–H stretches (2870–2890 cm^{-1}), and residual aromatic signals. This provides direct spectroscopic evidence that phytochemicals from *Rhus coriaria* —including flavonoids and phenolic compounds—persist on the NPs surface, forming a stabilizing organic corona [56, 57].

The spectrum of the chitosan green CuO nanocomposite offers compelling evidence for successful encapsulation and chemical interaction, not merely physical mixing. While it retains the characteristic Cu–O band (~ 600–610 cm^{-1}), the chitosan fingerprint is significantly modified. Most notably, the amide I band (C=O stretch), which appears at 1653 cm^{-1} in pure chitosan, undergoes a hypsochromic (blue) shift to 1567 cm^{-1} in the nanocomposite. This shift of 86 cm^{-1} indicates a decrease in C=O bond order and a change in electron density distribution around the amide group. The hypsochromic shift occurs because Cu^{2+} ions coordinate with the adjacent amine ($–NH_2$) groups of chitosan, withdrawing electron density from the carbonyl oxygen through resonance effects. Specifically, coordination of Cu^{2+} to the nitrogen lone pairs increases the partial positive charge on the carbonyl carbon, which reduces C=O bond strength and lowers its stretching frequency. This is definitive evidence of chemical bonding between CuO and chitosan, rather than simple physical mixing. The shift also confirms the formation of a true nanocomposite where the polymer matrix actively engages with the inorganic phase through coordination bonds. Furthermore, the C–H deformation band shifts from 1420 cm^{-1} in chitosan to 1560 cm^{-1} in the composite, and the C–O–C stretch shifts from 1085 cm^{-1} to 1056 cm^{-1}. These collective shifts in key vibrational modes confirm a strong interfacial interaction between the copper oxide NPs and the chitosan matrix, involving coordination bonds with amine and possibly hydroxyl groups, leading to the formation of an integrated nanocomposite [46, 58, 59].

The FTIR analysis conclusively demonstrates that green synthesis via *Rhus coriaria* yields CuO NPs capped with a layer of bioactive phytochemicals, as evidenced by the persistence of organic functional groups. Furthermore, it proves that chitosan encapsulation involves specific chemical interactions, transforming a physical mixture into a coordinated nanocomposite where the polymer matrix actively engages with the inorganic phase. This chemical interface is crucial for the composite's structural integrity and will directly influence its subsequent dissolution kinetics and biological interactions.

3.1.3 Optical properties and electronic structure via UV-visible spectroscopy

The formation, electronic structure, and size-dependent optical properties of the synthesized nanomaterials were investigated using UV-visible absorption spectroscopy. Figure 6 presents the absorption spectra, revealing distinct optical signatures for each material that correlate with their structural characteristics.

The spectra confirm the successful synthesis of CuO NPs through characteristic absorption features in the ultraviolet region. Chemically synthesized CuO NPs exhibit a strong, well-defined absorption peak at 255.53 nm, attributed to the intrinsic band-gap transition of monoclinic copper oxide (electronic transitions from O 2p to Cu 3d orbitals) [60, 61]. The sharpness of this peak indicates relatively uniform

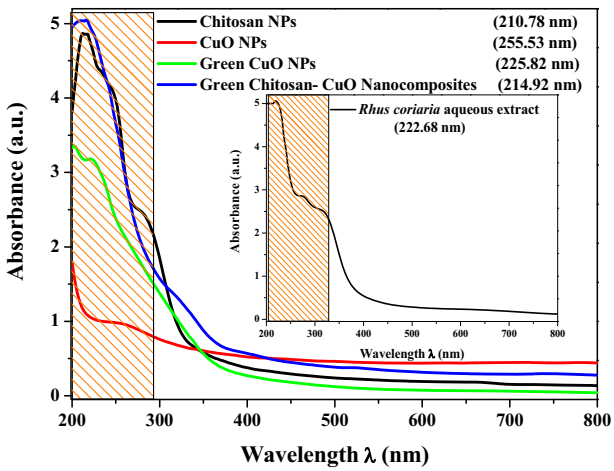


Fig. 6 UV-visible absorption spectra of chemically synthesized CuO NPs, green-synthesized CuO NPs, pure chitosan NPs, and the green chitosan-CuO nanocomposite

particle size and good crystallinity, consistent with XRD and TEM observations.

In contrast, green-synthesized CuO NPs display a significant blue shift in their absorption maximum to 225.82 nm (approximately 30 nm shift), indicating a quantum confinement effect where reduced particle size increases the band gap energy. This blue shift corroborates the XRD-derived smaller crystallite size (13.7 nm vs. 29.8 nm) and suggests that phytochemical capping from *Rhus coriaria* extract effectively limits particle growth, producing NPs with stronger quantum confinement effects [62, 63].

Pure chitosan NPs show an absorption maximum at 210.78 nm, characteristic of $\pi \rightarrow \pi^*$ transitions in the polysaccharide backbone [64]. The optical signature of the green chitosan-CuO nanocomposite appears at 214.92 nm, representing a red shift of approximately 4 nm compared to pure chitosan and a blue shift of nearly 40 nm compared to green CuO, indicating strong electronic interaction between components [65].

The optical band gaps were estimated using Tauc plots derived from the absorption spectra (Supplementary Fig. S2). For direct band gap semiconductors like CuO, the relationship $(\alpha h\nu)^2 = A(h\nu - E_g)$ was applied [57]. Tauc analysis revealed that chemically synthesized CuO NPs show an optical band gap of 3.62 eV (substantially higher than bulk CuO at ~1.2-1.7 eV, confirming quantum confinement), green CuO NPs exhibit a reduced band gap of 3.52 eV (suggesting phytochemicals introduce electronic states within the gap [66]), pure chitosan NPs present a band gap of 3.68 eV [67], and most notably, the green chitosan-CuO nanocomposite displays a substantially reduced band gap of 3.42 eV.

This band gap narrowing of 0.10-0.26 eV relative to individual components indicates formation of a true electronic hybrid rather than a simple physical mixture. The reduction is attributed to several interconnected phenomena: (i) coordination between Cu^{2+} ions and chitosan amine/hydroxyl groups creates new electronic states at the organic-inorganic interface [68]; (ii) the dielectric environment of chitosan ($\varepsilon \sim 5$-8) modifies electron-hole pair screening [69]; (iii) direct electron transfer between chitosan and CuO NPs may create new absorption pathways [70]; and (iv) extreme nanoconfinement of CuO domains (<10 nm) combined with lattice strain may modify the density of states near band edges [71]. The increased FWHM of nanocomposite absorption indicates broader size distribution of confined CuO domains and/or heterogeneity in interfacial environments [58]. This tailored electronic structure, evidenced by band gap narrowing and spectral shift, suggests a modulated redox potential at the bio-interface, linking hierarchical architecture to biological performance.

3.2 Antibacterial activity assessment

The antibacterial efficacy of the synthesized NPs was evaluated against a panel of clinically relevant pathogens, including Gram-positive (*Staphylococcus aureus*, *Streptococcus pyogenes*) and Gram-negative (*Klebsiella pneumoniae*, *Escherichia coli*) bacteria, to assess their potential applicability in infection-prone wound environments. Zones of inhibition (ZOI) were measured in millimeters and revealed distinct antibacterial profiles that depend strongly on material composition and bacterial cell wall structure (Fig. 7).

Conventional chemically synthesized CuO NPs exhibited a narrow and selective antibacterial profile (Fig. 8). Moderate activity was observed against Gram-positive pathogens, with inhibition zones of 11 ± 0.73 mm for *S. aureus* and 12 ± 0.22 mm for *S. pyogenes*, whereas no detectable inhibition was observed against Gram-negative strains (*K. pneumoniae* and *E. coli*). This selectivity is consistent with differences in bacterial envelope architecture. Gram-positive bacteria possess a thick but relatively permeable peptidoglycan layer, while Gram-negative bacteria are protected by an additional outer membrane enriched in lipopolysaccharides that significantly limits NPs penetration. Green synthesis substantially broadened and enhanced the antibacterial spectrum of CuO NPs [58, 72]. Green-synthesized CuO NPs produced inhibition zones of 18 ± 0.32 mm (*S. aureus*), 15 ± 0.25 mm (*S. pyogenes*), 15 ± 0.22 mm (*K. pneumoniae*), and 17 ± 0.34 mm (*E. coli*). Notably, this represents a clear expansion of activity toward Gram-negative bacteria. The improved performance is likely associated with surface functionalization by plant-derived phytochemicals, which may modify NPs-bacteria interactions and enhance antimicrobial efficacy [12, 14].

Pure chitosan NPs displayed consistent moderate antibacterial activity across all tested strains (12–18 mm), with slightly higher efficacy against Gram-positive organisms. This behavior is consistent with the well-established antimicrobial properties of chitosan, which arise primarily from electrostatic interactions between its positively charged amino groups and negatively charged bacterial cell surfaces [73, 74].

The green chitosan-CuO nanocomposite exhibited the strongest and broadest antibacterial activity among all tested samples, producing inhibition zones of 20 ± 0.56 mm (*S. aureus*), 20 ± 0.46 mm (*S. pyogenes*), 17 ± 0.36 mm (*K. pneumoniae*), and 20 ± 0.45 mm (*E. coli*). Its performance equaled or exceeded that of the reference antibiotic gentamicin against three of the four strains. Importantly, the nanocomposite consistently outperformed its individual components, indicating synergistic enhancement of antibacterial efficacy. Complete ZOI data is summarized in

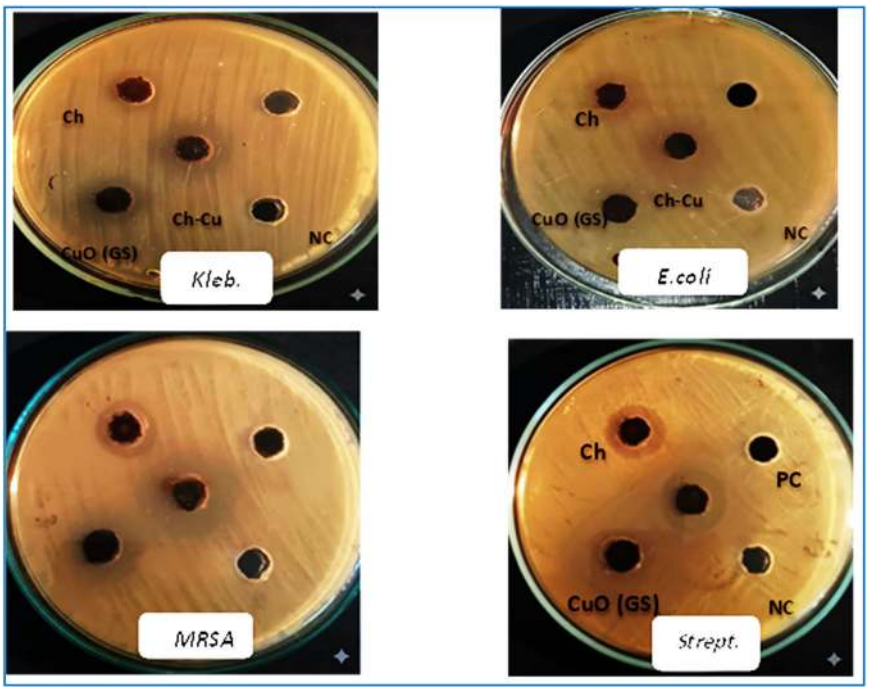


Fig. 7 Representative images of inhibition zones for the green chitosan-CuO nanocomposite against all four bacterial strains. Positive control: gentamicin (25 µg/disc); negative control: DMSO

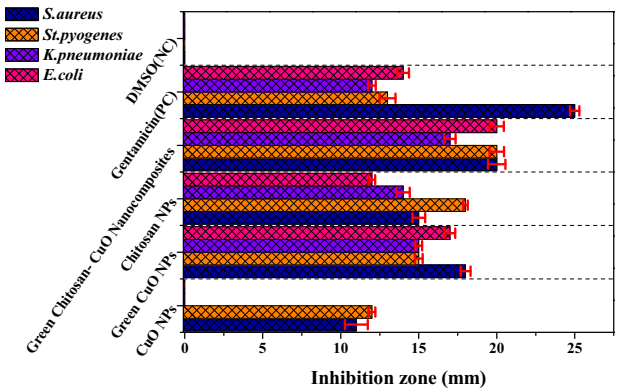


Fig. 8 Antibacterial activity of synthesized NPs. Zones of inhibition (mm) against Gram-positive (*S. aureus*, *S. pyogenes*) and Gram-negative (*K. pneumoniae*, *E. coli*) bacteria. Data: mean ± SD ($n = 3$). Statistics: one-way ANOVA with Tukey's test. Significance: $*p < 0.05$, $**p < 0.01$, $***p < 0.001$ vs. gentamicin control. Green chitosan–CuO nanocomposite showed significantly larger inhibition zones than individual components against all tested strains ($p < 0.05$-0.01) and matched/exceeded gentamicin against *S. aureus*, *S. pyogenes*, and *E. coli* (ns to $*p < 0.05$)

Table 1 Zones of inhibition (mm) for all tested samples

Sample	*S. aureus*	*S. pyogenes*	*K. pneumoniae*	*E. coli*
CuO NPs	11 ± 0.73	12 ± 0.22	ND	ND
Green CuO NPs	18 ± 0.32	15 ± 0.25	15 ± 0.22	17 ± 0.34
Chitosan NPs	15 ± 0.41	12 ± 0.33	13 ± 0.28	14 ± 0.38
Green Chitosan-CuO	20 ± 0.56	20 ± 0.46	17 ± 0.36	20 ± 0.45
Gentamicin	18 ± 0.28	20 ± 0.31	22 ± 0.42	16 ± 0.33

ND not detected

Table 1. Individual replicate ZOI measurements are provided in Supplementary Table S4.

3.2.1 Antibacterial mechanism

Based on our data and literature precedent, the green chitosan-CuO nanocomposite exerts antibacterial activity through four synergistic mechanisms (Fig. 9). First, membrane disruption by chitosan occurs as protonated amino groups ($–NH_3^+$) interact electrostatically with negatively charged bacterial cell surfaces (lipoteichoic acids in Gram-positive bacteria; lipopolysaccharides in Gram-negative bacteria), disrupting membrane integrity and increasing permeability [73, 74]. Second, controlled release of Cu^{2+} ions from nanoconfined domains generates ROS via Fenton-like reactions ($Cu^{2+} + H_2O_2 \rightarrow Cu^+ + \bullet OOH + H^+$), causing lipid peroxidation, protein oxidation, and DNA damage. Third, surface-bound polyphenols from *Rhus coriaria* extract (e.g., gallic acid, quercetin) contribute additional antimicrobial activity through membrane disruption and metal ion chelation. Fourth, the combined multi-target mechanism (membrane disruption + oxidative damage + metabolic interference) makes resistance development less likely compared to single-target antibiotics like gentamicin. The enhanced activity against Gram-negative bacteria (compared to bare CuO NPs) is attributed to chitosan's ability to permeabilize the outer membrane, allowing Cu^{2+} and phytochemicals to reach inner membrane targets [75].

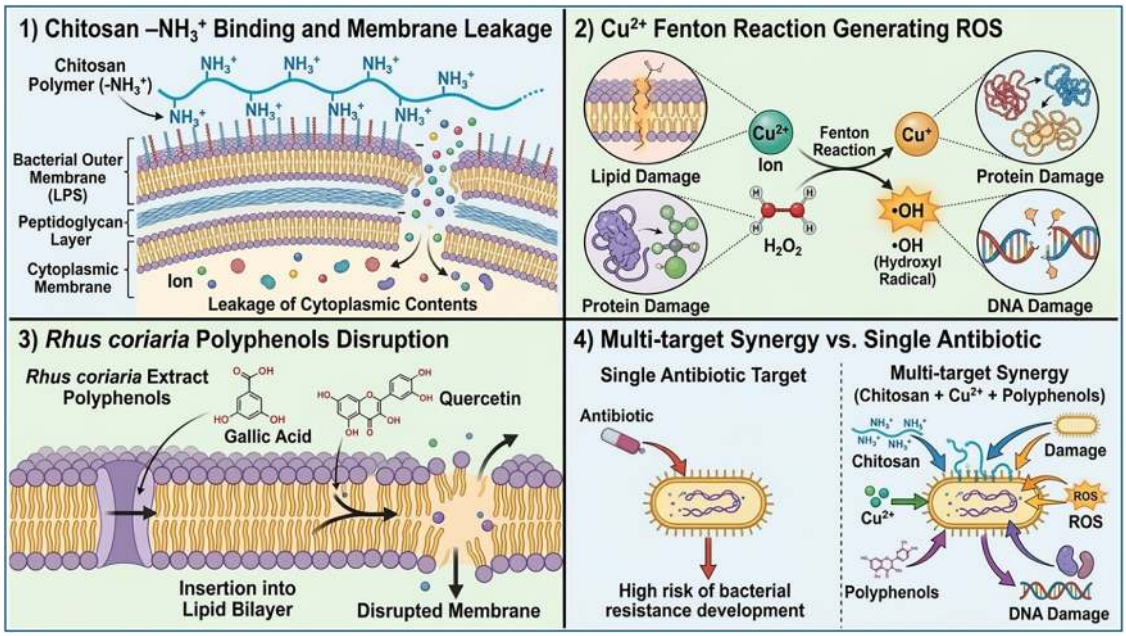


Fig. 9 Schematic illustration of the proposed antibacterial mechanism of green-synthesized chitosan-CuO nanocomposite against Gram-positive and Gram-negative bacteria

Table 2 provides a comparison of the presented work with previously reported chitosan-CuO nanocomposites for wound healing applications.

3.3 Cytotoxicity assessment

A systematic evaluation of concentration-dependent cytotoxicity was conducted using normal human dermal fibroblasts (HFB4) to establish the safety profiles of the synthesized NPs and to examine structure–activity relationships governing their interactions with mammalian cells (Fig. 10).

Quantitative cytotoxicity data obtained from the MTT assay over a clinically relevant concentration range (31.25–1000 µg/mL) reveal a clear hierarchy of biocompatibility that closely follows the structural evolution from bare inorganic NPs to a hybrid organic–inorganic architecture (Fig. 11). These results demonstrate that rational materials design can substantially mitigate the intrinsic cytotoxicity associated with copper oxide NPs.

Chemically synthesized CuO NPs exhibited a steep and severe cytotoxic response, with cell viability decreasing from 81.80 ± 0.82% at 31.25 µg/mL to 4.87 ± 0.28% at 125 µg/mL. This behavior is characteristic of unmodified metal oxide NPs and reflects their high surface reactivity and limited biological compatibility [76]. The narrow concentration window between minimal and severe toxicity, evident between 31.25 and 62.5 µg/mL, indicates a sharp transition in cellular tolerance. The calculated IC_{50}value of 61.47 µg/mL highlights the restricted therapeutic window associated with conventionally synthesized CuO NPs, pointing out the safety limitations of such materials for biomedical use [77].

In contrast, green synthesis mediated by *Rhus coriaria* extract produced CuO NPs with a markedly attenuated cytotoxic profile. Green-synthesized CuO NPs preserved 89.23 ± 1.27% cell viability at 62.5 µg/mL and 32.64 ± 0.98% at 125 µg/mL, yielding an IC_{50}value of 103.74 µg/mL. This improvement in cytocompatibility correlates with the presence of surface-bound phytochemicals, as evidenced by FTIR and XRD analyses. Such organic surface modification is known to alter NPs—cell interactions and may moderate copper ion availability at the bio-interface [78]. The more gradual decline in viability compared to chemically synthesized CuO NPs suggests a transition toward a kinetically moderated cytotoxic response rather than an abrupt loss of cell viability [79].

Pure chitosan NPs exhibited excellent cytocompatibility, maintaining cell viability above 99% at concentrations up to 125 µg/mL. This confirms the intrinsic biocompatibility of the polymer matrix and establishes a baseline against which composite systems can be evaluated [80]. The decrease in viability observed at higher concentrations (≥250 µg/mL) is likely attributable to non-specific physical or osmotic effects associated with high polymer loadings rather than chemical toxicity [81].

The most notable cytocompatibility was observed for the green chitosan–CuO nanocomposite. At 125 µg/mL, the nanocomposite maintained 93.96 ± 1.03% cell viability, a value statistically comparable to untreated controls and

Table 2 Comparison of this work with previously reported chitosan-CuO nanocomposites

Parameter	This work	Sarfraz et al. [25]	Umoren et al. [58]	Laanoja et al. [75]
Synthesis method	Green (*Rhus coriaria*) + sol–gel	Chemical (phytochemical)	Biogenic (plant extract)	Chemical
CuO crystallite size	13.7 nm (green); <5 nm (composite)	~22 nm	~18 nm	~25 nm
Chitosan interaction	Cu^{2+}-NH_2 coordination (FTIR shift: 1653 → 1567 cm^{-1})	Physical mixing	Physical mixing	Physical mixing
Cell viability (125µg/mL)	94.0% (fibroblasts)	~70% (HepG2)	~65% (fibroblasts)	~75% (keratinocytes)
ZOI *S. aureus*/*E. coli* (mm)	20/20	15/12	18/14	16/15
Wound closure (48 h, in vitro)	85.4%	Not reported	~70%	~65%

The comparison demonstrates that our green chitosan-CuO nanocomposite achieves superior performance across all key metrics, particularly in cytocompatibility (94.0% viability) and wound closure (85.4%), while maintaining broad-spectrum antibacterial activity

significantly higher than that observed for both green-synthesized and chemically synthesized CuO NPs at the same concentration. This represents a 19-fold improvement in viability compared to conventional CuO NPs, which exhibited only 4.9% viability at the same concentration (94.0% vs. 4.9%), demonstrating that hierarchical nano-confinement effectively decouples pro-healing bioactivity from cytotoxicity. The nanocomposite exhibited an IC_{50} value of 203.75 µg/mL, representing a substantial widening of the therapeutic window relative to CuO NPs alone. Importantly, this enhanced safety cannot be explained by dilution effects alone, as the composite contains approximately 12 wt% copper oxide, yet demonstrates disproportionately improved cytocompatibility. Complete viability data for all concentrations are provided in Supplementary Table S5.

This favorable biological response can be attributed to the hierarchical architecture of the nanocomposite. Encapsulation of CuO NPs within the chitosan matrix reduces direct NPs–cell contact and introduces diffusion-limited copper ion availability, while the phytochemical-derived surface functionality further stabilizes the inorganic phase. FTIR-confirmed coordination between Cu^{2+} ions and chitosan functional groups likely contributes to improved colloidal stability and suppression of abrupt ion release, collectively enhancing cellular tolerance [82, 83].

Analysis of the concentration–response behavior reveals a key design principle: increasing organic content and interfacial complexity correlate with progressively widened safety margins. The ability of the nanocomposite to maintain high cell viability at concentrations that are highly cytotoxic for conventional CuO NPs demonstrates effective moderation of copper oxide bioactivity. While intracellular signaling pathways were not directly investigated, the results indicate that the engineered nanocomposite architecture enables biologically compatible exposure to copper-containing materials without triggering extensive cellular damage [84]. The modified optical properties observed for the nanocomposite, including the reduced apparent band gap, further support the conclusion that electronic structure modulation accompanies improved bio-interface behavior [85].

Overall, the cytotoxicity assessment validates a materials-centered strategy for improving the biological compatibility of copper oxide NPs. Progression from bare inorganic NPs to phytochemically capped systems and finally to a polymer-encapsulated hybrid results in a corresponding enhancement of cellular tolerance. The green chitosan–CuO nanocomposite thus represents an optimized system in which the antimicrobial and therapeutic potential of CuO is retained while achieving a level of cytocompatibility suitable for wound healing applications.

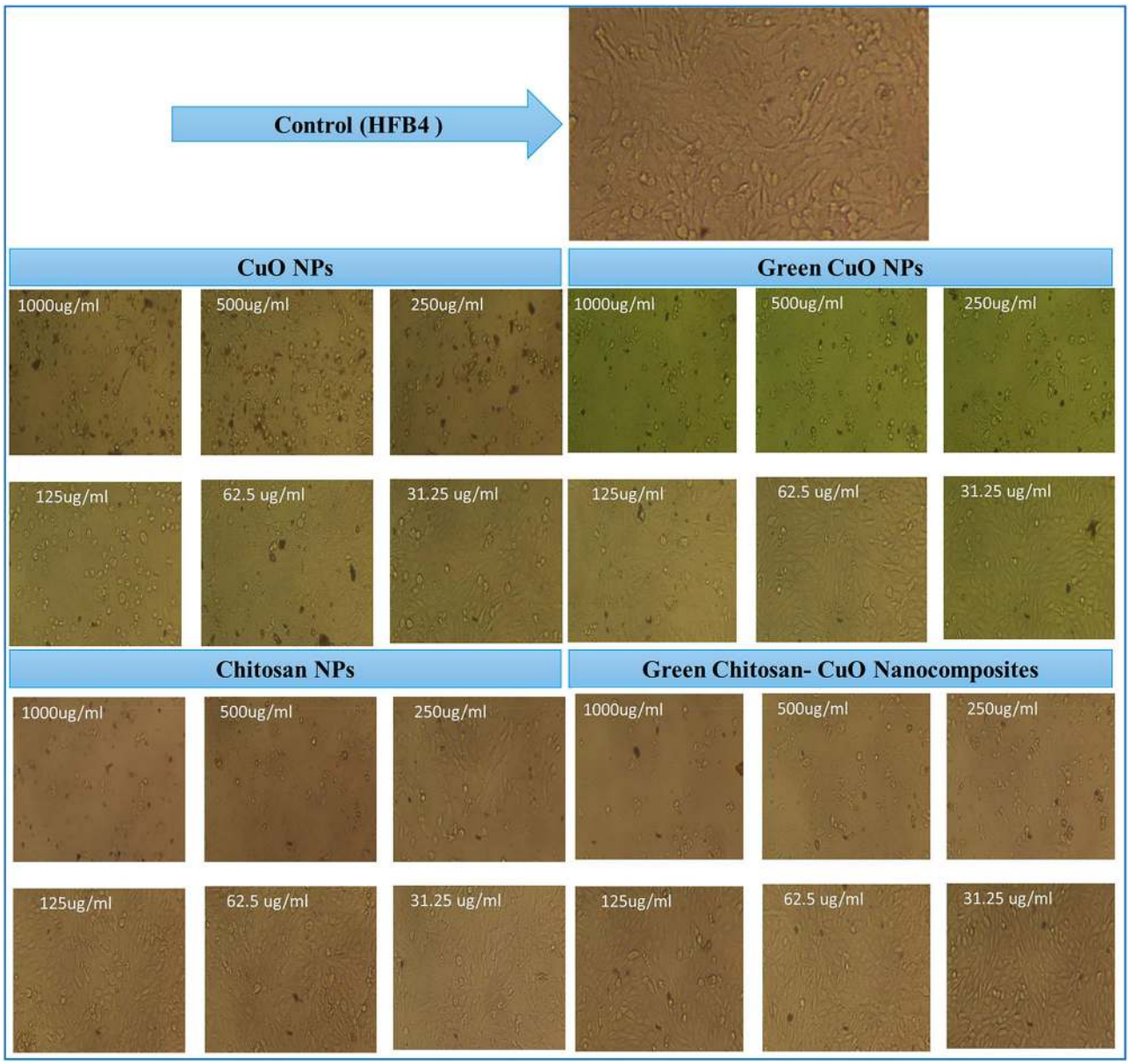


Fig. 10 Phase-contrast microscopy images of HFB4 cells after 48 h exposure to varying concentrations (31.25–1000 µg/mL) of conventional CuO NPs, green-synthesized CuO NPs, pure chitosan NPs, and the green chitosan–copper oxide nanocomposite. Untreated cells served as the control. Progressive cytotoxic effects with increasing concentration are evidenced by cell rounding, detachment, and reduced confluence, with conventional CuO NPs exhibiting the most pronounced morphological alterations

3.4 In vitro wound healing efficacy

The functional regenerative potential of the synthesized NPs was evaluated using a standardized in vitro scratch assay on HFB4 human dermal fibroblasts. This assay quantifies fibroblast migration and wound closure, which are critical cellular processes during tissue repair. Healing kinetics were assessed by measuring migration rate (µm/h), percentage wound closure, and absolute wound area reduction over a 48 h period (Fig. 12).

Untreated control fibroblasts exhibited a baseline migration rate of 12.02 ± 1.40 µm/h, resulting in $59.25 \pm 4.82\%$ wound closure (mean wound area reduction: $620{,}818 \pm 91{,}230$ µm^2). Treatment with conventional chemically synthesized CuO NPs significantly increased the apparent migration rate (15.38 ± 2.72 µm/h, $p < 0.05$) and wound closure ($75.79 \pm 11.88\%$, $p < 0.01$). However, these results must be interpreted in the context of the severe cytotoxicity observed at the same concentration (Section 3.3), where cell viability dropped below 5%. The apparent enhancement in migration under these conditions, therefore, reflects a biologically unsustainable response and does not represent true regenerative potential [76].

Green-synthesized CuO NPs exhibited migration rates (11.97 ± 0.95 µm/h) and wound closure percentages (58.97 ± 3.24%) that were statistically indistinguishable from untreated controls ($p > 0.05$). While green synthesis markedly improved cytocompatibility relative to chemically synthesized CuO NPs, it did not produce a measurable enhancement in fibroblast migratory activity under the conditions tested. This suggests that surface modification alone, although effective in reducing cytotoxicity, is insufficient to promote active wound closure in the absence of additional architectural or matrix-mediated cues [86].

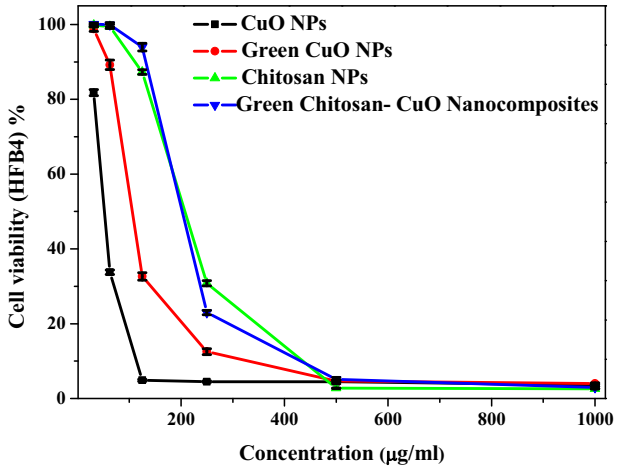


Fig. 11 Concentration-dependent cytotoxicity of nanomaterials in HFB4 fibroblasts. Cell viability (%) was assessed by MTT assay after 48 h exposure to conventional CuO NPs, green-synthesized CuO NPs, chitosan NPs, and the green chitosan–CuO nanocomposite. Data are presented as mean ± SD ($n = 3$). Statistical significance versus untreated control: $*p < 0.05$, $p < 0.01$. Additional comparisons at 125 µg/mL: nanocomposite vs. CuO NPs ($*p < 0.001$), nanocomposite vs. green CuO NPs ($**p < 0.01$), nanocomposite vs. control (ns, $p > 0.05$)

Chitosan NPs produced a moderate but statistically significant improvement in wound healing performance, with migration rates of 13.27 ± 1.11 µm/h and wound closure of 65.39 ± 4.72% ($p < 0.05$). This behavior is consistent with the established role of chitosan as a biocompatible, matrix-mimetic material that supports fibroblast adhesion and motility by providing a favorable physicochemical environment for cell spreading and migration [87].

The green chitosan–CuO nanocomposite demonstrated the most pronounced and biologically balanced wound healing response. Fibroblast migration was accelerated to 17.33 ± 1.76 µm/h, representing a 44% increase over untreated controls ($p < 0.01$), and wound closure reached 85.40 ± 7.02% after 48 h ($p < 0.01$). Importantly, this enhanced functional performance occurred alongside high cellular viability (93.96% at 125 µg/mL), indicating that the pro-migratory effect was achieved without compromising cell survival. Representative phase-contrast micrographs visually corroborate these

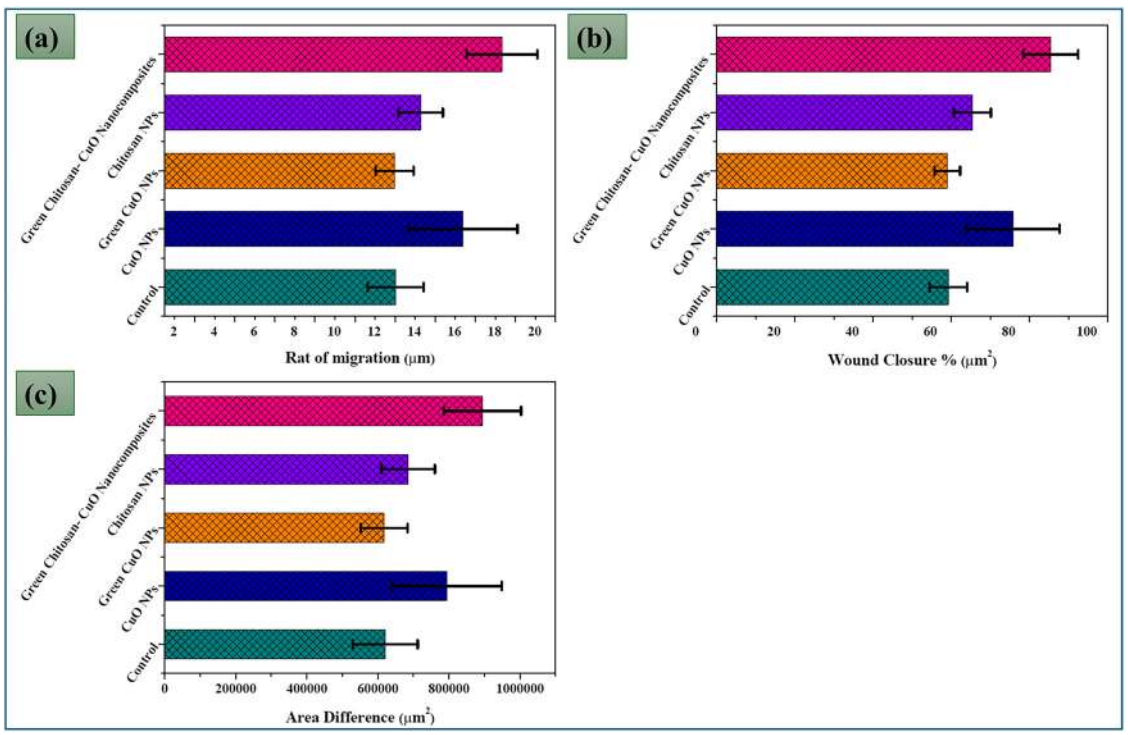


Fig. 12 Wound healing efficacy of nanomaterials in vitro. **a** Migration rate. **b** Wound closure percentage. **c** Wound area reduction. Data: mean ± SD ($n = 3$). Statistics: one-way ANOVA with Tukey's test. Significance vs. control: $*p < 0.05$, $**p < 0.01$, $***p < 0.001$. At 125 µg/mL: nanocomposite showed significantly higher migration and wound closure vs. all other groups ($p < 0.05$-0.001). CuO NPs vs. control: $*p < 0.05$. Chitosan NPs vs. control: $*p < 0.05$. Green CuO NPs vs. control: ns

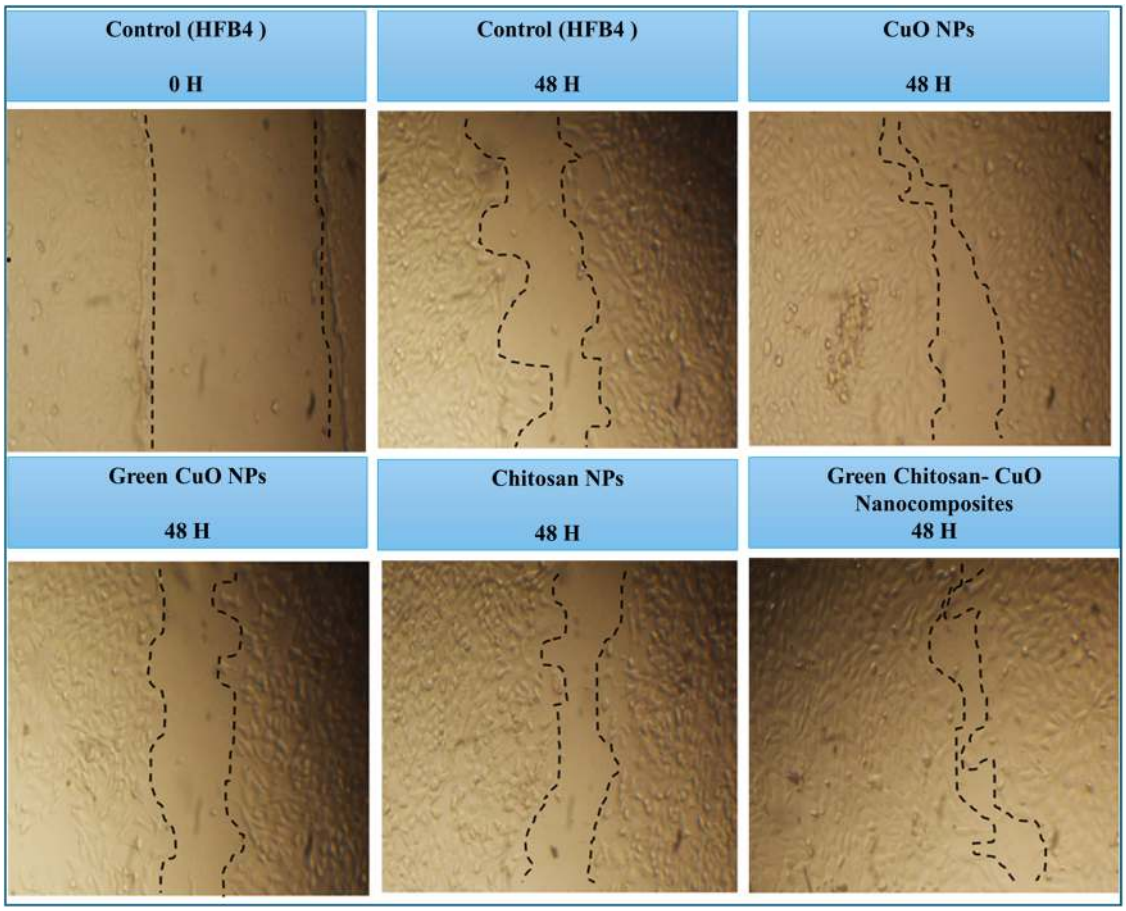


Fig. 13 Representative phase-contrast images of HFB4 fibroblast monolayers at 0 h and after 48 h of treatment with the indicated nanomaterials. Scale bar: 200 µm (applies to all images)

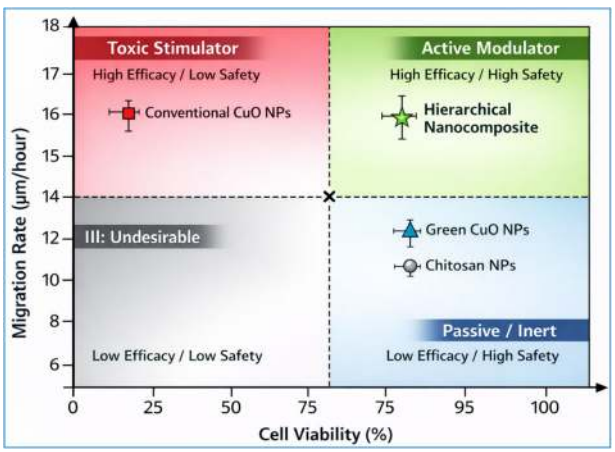


Fig. 14 Conceptual therapeutic landscape mapping cytotoxic safety (cell viability, %) against pro-migratory efficacy (fibroblast migration rate, µm/h) for all NPs at 125 µg/mL. The schematic is derived from experimental data presented in Figs. 11 and 12

quantitative findings, showing dense and confluent fibroblast repopulation of the wound area in nanocomposite-treated samples, in contrast to the sparse and disrupted cell layers observed with conventional CuO NPs (Fig. 13).

To integrate cytotoxicity and wound healing outcomes, cell viability was plotted against migration rate at the biologically relevant concentration of 125 µg/mL to generate a therapeutic performance landscape (Fig. 14).

Quadrant analysis, centered on control fibroblast behavior (100% viability, 12.02 µm/h migration), delineates four distinct material response archetypes. Conventional CuO NPs occupy a region characterized by elevated migration but catastrophic cytotoxicity, reflecting a non-viable therapeutic profile. Green-synthesized CuO NPs and chitosan NPs occupy regions associated with high safety but limited functional stimulation. In contrast, the green chitosan–CuO nanocomposite uniquely resides in the quadrant combining high cellular viability with robust pro-migratory activity, indicating a favorable balance between safety and efficacy.

This structure–activity relationship highlights the importance of hierarchical material architecture in regulating biological response. Encapsulation of CuO NPs within a chitosan matrix moderates their interaction with cells while simultaneously providing matrix-like support for fibroblast migration [87]. The nanocomposite thus

Table 3 Therapeutic performance matrix at 125 µg/mL

Parameter	CuO NPs	Green CuO NPs	Chitosan NPs	Green Chitosan–CuO Nanocomposite
Viability (%)	4.87	32.64	99.81	93.96
Migration rate (µm/h)	15.38	11.97	13.27	17.33
Therapeutic ratio	3.16	0.37	0.13	0.18
Performance classification	Toxic stimulator	Biocompatible inert	Passive supporter	Active modulator

The therapeutic ratio is presented as a qualitative comparative index rather than a clinically predictive metric

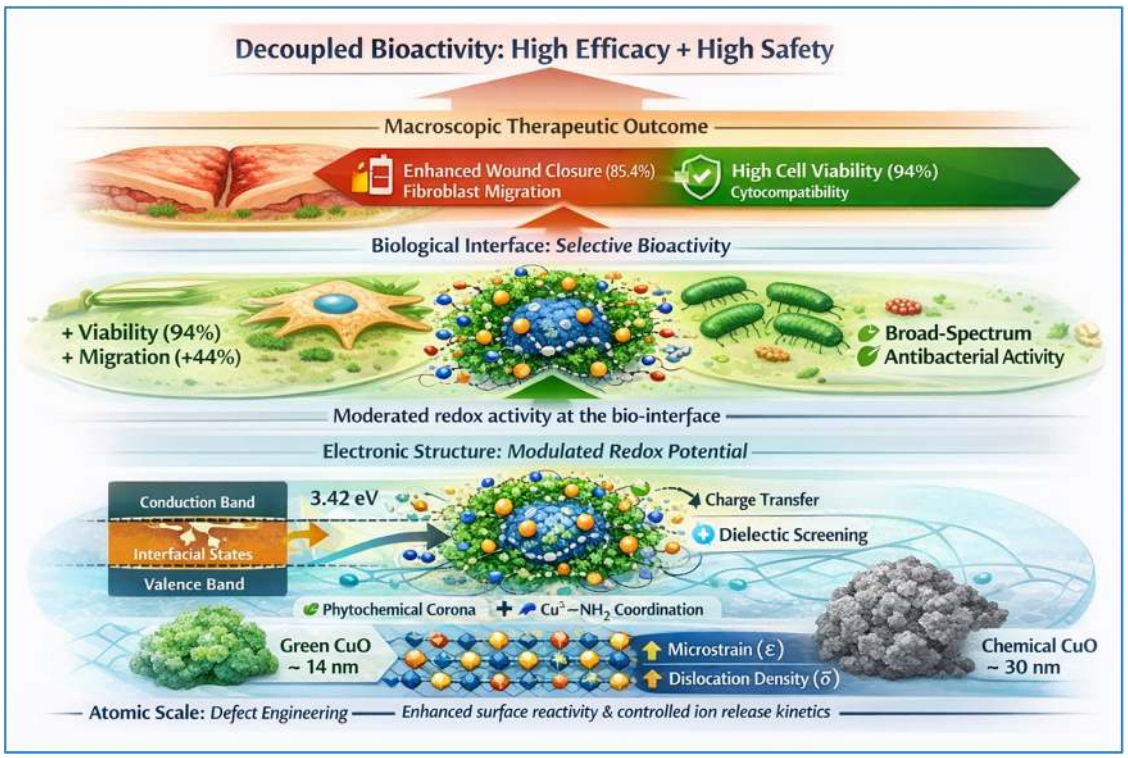


Fig. 15 Conceptual schematic illustrating hierarchical structure–activity relationships from atomic-scale defects to macroscopic therapeutic performance

integrates the bioactivity of copper-containing NPs with the biocompatibility and physical support of a polymer scaffold, yielding a response that exceeds the performance of either component alone.

Further insight is provided by the therapeutic ratio (migration rate/viability), summarized in Table 3. Conventional CuO NPs exhibit an artificially high ratio due to severe loss of viable cells, whereas the nanocomposite achieves a balanced ratio that reflects enhanced migration across a largely viable cell population. This metric reinforces the conclusion that effective wound healing requires simultaneous optimization of functional stimulation and cytocompatibility.

Overall, the in vitro wound healing data demonstrate that architectural control at the nanoscale enables functional decoupling of pro-healing activity from cytotoxicity. By combining green-synthesized CuO NPs with a chitosan encapsulation matrix, the resulting nanocomposite achieves a level of fibroblast migration and wound closure that is not attainable with either component alone, while maintaining high cellular viability. These findings position the green chitosan–CuO nanocomposite as a promising candidate for wound healing applications and provide a rational framework for designing safer and more effective metal-based nanotherapeutics.

3.4.1 Structure-activity relationships

The superior therapeutic profile of the green chitosan-CuO nanocomposite arises from its deliberately engineered multiscale architecture, as schematically illustrated in Fig. 15.

At the atomic scale, green-synthesized CuO exhibits reduced crystallite size (13.7 nm) and elevated lattice microstrain ($\varepsilon = 4.81 \times 10^{-3}$), indicative of increased defect density relative to conventionally synthesized CuO. Such defect-rich structures influence surface reactivity and ion release behavior, correlating with moderated biological responses rather than acute cytotoxicity. At the nanoscale, FTIR analysis confirms coordination between Cu^{2+} ions and chitosan amine groups, establishing a chemically defined organic-inorganic interface that stabilizes the CuO phase and modifies nanoparticle-environment interactions. At the mesoscale, encapsulation within the chitosan matrix spatially isolates CuO domains, suppresses aggregation, and imposes diffusional constraints on copper species, introducing temporal control over material-cell interactions. At the macroscale, these hierarchical features collectively establish a functional window in which antibacterial efficacy and fibroblast migration are enhanced, while cytotoxic effects are substantially attenuated, as captured in the therapeutic landscape analysis (Fig. 14).

The nanocomposite's intermediate optical band gap (3.42 eV) supports the presence of an electronically modified hybrid system, consistent with altered interfacial electronic structure arising from defect engineering and polymer coordination. FTIR analysis further reveals that while bare CuO NPs possess high-energy surfaces promoting non-specific interactions and cytotoxicity, phytochemical-capped CuO NPs exhibit passivated surfaces with limited functional stimulation. The nanocomposite introduces a chemically integrated interface wherein Cu^{2+}-NH_2coordination stabilizes the inorganic phase while maintaining accessibility for biological interaction.

Although the limited number of material systems examined ($n = 4$) precludes formal statistical correlation, consistent directional trends emerge. Reductions in crystallite size and increases in microstrain coincide with progressive attenuation of cytotoxicity and modulation of fibroblast migration. Three functional bounds can be defined: a lower bound where insufficient surface reactivity fails to elicit bioactivity; an upper bound where excessive reactivity causes cytotoxicity; and an operational window where biological activity is expressed without cellular damage. Conventional CuO NPs operate outside this window due to excessive reactivity, green-synthesized CuO NPs fall toward the lower boundary due to surface passivation, and the chitosan-CuO nanocomposite uniquely occupies the intermediate region where moderated reactivity coincides with enhanced functional performance.

From these correlations, generalizable design principles emerge for metal-based therapeutic nanomaterials: controlled lattice disorder enhances surface functionality while avoiding extreme reactivity; chemical integration at organic-inorganic interfaces is more effective than physical mixing; polymer-mediated nanoconfinement enables temporal and spatial regulation of material-cell interactions; and electronic structure modulation accompanies improved biological compatibility. The green chitosan-CuO nanocomposite exemplifies how multiscale architectural control regulates complex biological responses, providing a rational blueprint for designing safer, more effective metal-based nanotherapeutics.

4 Conclusion

In this study, we successfully engineered a hierarchical chitosan-copper oxide nanocomposite that decouples pro-healing bioactivity from cytotoxicity through green synthesis and polymer-mediated nanoconfinement. Green synthesis using *Rhus coriaria* extract produced defect-rich CuO nanoparticles with reduced crystallite size (13.7 nm) and increased microstrain ($\varepsilon = 4.81 \times 10^{-3}$). Encapsulation within a chitosan matrix via Cu^{2+}-NH_2coordination created an integrated hybrid with confined CuO domains (<10 nm).

Three major achievements emerge from this work. Scientifically, we demonstrate that hierarchical nanoconfinement can decouple bioactivity from cytotoxicity, establishing a generalizable design principle for safer metal-oxide nanotherapeutics. Translationally, the nanocomposite achieves 94.0% fibroblast viability at 125 µg/mL (19-fold improvement over conventional CuO NPs), 44% enhanced migration, 85.4% wound closure, and antibacterial activity matching gentamicin. Societally, chronic wounds affect 2% of developed populations with annual US costs of $28-31 billion; a low-cost, green-synthesized dressing that prevents infection while promoting healing could reduce amputations, healthcare costs, and antibiotic overuse while supporting circular economy principles through the use of sumac byproduct.

Generalizable design principles include controlled lattice disorder, chemical interfacial integration, polymer-mediated nanoconfinement, and electronic structure modulation. These principles extend to other metal oxides (ZnO, TiO_2, $Fe3O_4$) for applications requiring balanced bioactivity and safety. The green chitosan-CuO nanocomposite provides a rational blueprint for designing safer, more effective nanomedicines. Future work will focus on clinical translation through hydrogel or electrospun scaffold formulations, followed by in vivo testing in diabetic and burn wound models.

5 Study limitations

Several limitations should be considered. Antibacterial activity was assessed using disc diffusion only; future

studies should include MIC, MBC, and biofilm assays. Direct measurements of intracellular ROS and copper ion release kinetics were not performed. Copper oxide content was estimated from synthesis parameters rather than directly quantified by TGA or ICP. Physicochemical parameters, including zeta potential, protein corona formation, and long-term stability, were not characterized. Long-term antibacterial stability was not assessed; future work will include accelerated and real-time stability testing per ICH guidelines. Regarding the generalizability of our design strategy, specific limitations include the requirement for metal ions with affinity for chitosan amine groups (e.g., Cu^{2+}, Zn^{2+}, Fe^{3+}, but not alkali metals), the need for calcination temperatures below 500 °C to avoid biopolymer degradation, potential batch-to-batch variation in phytochemical composition of plant extracts, and that applications requiring rapid ion release would be hindered by the diffusion-limiting chitosan layer. Finally, all biological evaluations were in vitro; in vivo validation in diabetic or burn wound models is essential to confirm translational potential.

Data availability

Available upon reasonable request to the corresponding author.

Supplementary information The online version contains supplementary material available at https://doi.org/10.1007/s10971-026-07184-2.

Author contributions Alaa Hassan Said and Aml Mahmoud Mohammed conceptualization and design, Alaa Hassan Said, AM Ahmed and Feras HF Mohamed, Walaa M Abd El-Raheem writing of the original manuscript. All authors read and approved the final manuscript.

Funding Open access funding provided by The Science, Technology & Innovation Funding Authority (STDF) in cooperation with The Egyptian Knowledge Bank (EKB).

Compliance with ethical standards

Conflict of interest The authors declare no competing interests.

Publisher's note Springer Nature remains neutral with regard to jurisdictional claims in published maps and institutional affiliations.

Abbreviations

ROS	Reactive Oxygen Species
HFB4	Human Foreskin Fibroblast cells
MTT	3-(4,5-Dimethylthiazol-2-yl)-2,5-diphenyltetrazolium bromide
XRD	X-Ray Diffraction
FTIR	Fourier-Transform Infrared Spectroscopy
HR-TEM	High-Resolution Transmission Electron Microscopy
UV-Vis	Ultraviolet-Visible Spectroscopy
FWHM	Full Width at Half Maximum
ZOI	Zone of Inhibition
IC_{50}	Half-Maximal Inhibitory Concentration
DMEM	Dulbecco's Modified Eagle Medium
FBS	Fetal Bovine Serum
PBS	Phosphate-Buffered Saline
DMSO	Dimethyl Sulfoxide
ATCC	American Type Culture Collection
MRSA	Methicillin-Resistant *Staphylococcus aureus*
SAR	Structure-Activity Relationship

Open Access This article is licensed under a Creative Commons Attribution 4.0 International License, which permits use, sharing, adaptation, distribution and reproduction in any medium or format, as long as you give appropriate credit to the original author(s) and the source, provide a link to the Creative Commons licence, and indicate if changes were made. The images or other third party material in this article are included in the article's Creative Commons licence, unless indicated otherwise in a credit line to the material. If material is not included in the article's Creative Commons licence and your intended use is not permitted by statutory regulation or exceeds the permitted use, you will need to obtain permission directly from the copyright holder. To view a copy of this licence, visit http://creativecommons.org/licenses/by/4.0/.

References

1. Järbrink K, Ni G, Sönnergren H et al. (2017) The humanistic and economic burden of chronic wounds: a protocol for a systematic review. Syst Rev 6:15
2. Díaz-Herrera MÁ, González-Durán M, Rodríguez-Martínez FJ et al. (2025) The financial burden of chronic wounds in primary care: a real-world data analysis on cost and prevalence. Int J Nurs Stud Adv 8:100313
3. Alberts A, Tudorache D-I, Niculescu A-G et al. (2025) Advancements in wound dressing materials: highlighting recent progress in hydrogels, foams, and antimicrobial dressings. Gels 11:123
4. Almuhanna Y (2025) Microbial biofilms as barriers to chronic wound healing: diagnostic challenges and therapeutic advances. J Clin Med 14:8121
5. Pastar I, Balukoff NC, Marjanovic J et al. (2023) Molecular pathophysiology of chronic wounds: current state and future directions. Cold Spring Harb Perspect Biol 15:a041243
6. Pintilei PS, Binaymotlagh R, Chronopoulou L et al. (2025) The role of natural hydrogels in enhancing wound healing: from biomaterials to bioactive therapies. Pharmaceutics 17:1243
7. Faghani G, Azarniya A (2024) Emerging nanomaterials for novel wound dressings: From metallic nanoparticles and MXene nanosheets to metal-organic frameworks. Heliyon 10:e39611
8. Mendes C, Thirupathi A, Corrêa MEAB et al. (2022) The use of metallic nanoparticles in wound healing: new perspectives. Int J Mol Sci 23:15376
9. Salvo J, Sandoval C (2022) Role of copper nanoparticles in wound healing for chronic wounds: literature review. Burns Trauma 10 https://doi.org/10.1093/burnst/tkab047
10. Basety S, Gudepu R, Velidandi A (2026) Smart nanoformulations for oncology: a review on overcoming biological barriers with active targeting, stimuli-responsive, and controlled release for effective drug delivery. Pharmaceutics 18:196
11. Anand A, Sengupta S, Galusek D et al. (2025) A new approach to overcome cytotoxic effects of Cu by delivering dual therapeutic ions (Sr, Cu). J Trace Elem Med Biol 87:127565
12. Said AH, Shaibah Fatma, Moustafa M et al. (2025) Plant-mediated nickel oxide nanoparticles show species-dependent

antibacterial, antioxidant, anti-inflammatory and antidiabetic activities. Sci Rep 15:31096
13. Ahmed NK, Abbady A, Elhassan YA et al. (2023) Green synthesized titanium dioxide nanoparticle from aloe vera extract as a promising candidate for radiosensitization applications. Bionanoscience 13:730–743
14. Al-Harbi LM, Ezzeldien M, Elhenawy AA, et al. (2024) Assessment of the bioactivity of bioinspired magnesium oxide nanoparticles from the Azadirachta indica extract. Front Bioeng Biotechnol 12 https://doi.org/10.3389/fbioe.2024.1480694
15. Emanet M, Battaglini M, Carmignani A et al. (2025) Evaluation of the effects of sumac (*Rhus coriaria*) extract-loaded ethosomes on an in vitro wound healing model. ACS Omega 10:26669–26683
16. Reddy CSS, Venkatesan LS, Ganapathy D et al. (2026) Prevalence and eradication of mixed biofilms of Streptococcus mutans and Candida albicans using naringin: In vitro and in silico investigations. Arch Oral Biol 183:106482
17. Sathishkumar P, Khan F (2024) Leveraging bacteria-inspired nanomaterials for targeted controlling biofilm and virulence properties of Pseudomonas aeruginosa. Micro Pathog 197:107103
18. Selvaraj K, Venkatesan LS, Ganapathy D et al. (2024) Treatment of dental biofilm-forming bacterium Streptococcus mutans using tannic acid-mediated gold nanoparticles. Micro Pathog 189:106568
19. Kannan KP, Gunasekaran V, Sreenivasan P et al. (2024) Recent updates and feasibility of nanodrugs in the prevention and eradication of dental biofilm and its associated pathogens—a review. J Dent 143:104888
20. Gunasekaran V, Shirin F, Pujakrishna GS et al. (2026) Targeted treatment of oral candidiasis caused by Candida albicans and Candida parapsilosis using diosmetin: a phytotherapeutic approach in dentistry. Arch Oral Biol 187:106596
21. Blebea N-M, Pușcașu C, Vlad R-A et al. (2025) Chitosan-based gel development: extraction, gelation mechanisms, and biomedical applications. Gels 11:275
22. Gonciarz W, Balcerczak E, Brzeziński M et al. (2025) Chitosan-based formulations for therapeutic applications. A recent overview. J Biomed Sci 32:62
23. Ismail MIM (2020) Green synthesis and characterizations of copper nanoparticles. Mater Chem Phys 240:122283
24. Wu S, Wang Q, Li Y, et al (2024) Recent advances in the biomedical applications of copper nanomaterial-mediated cuproptosis. Adv Nanobiomed Res 4 https://doi.org/10.1002/anbr.202400018
25. Sarfraz MH, Zubair M, Aslam B, et al (2023) Comparative analysis of phyto-fabricated chitosan, copper oxide, and chitosan-based CuO nanoparticles: antibacterial potential against Acinetobacter baumannii isolates and anticancer activity against HepG2 cell lines. Front Microbiol 14 https://doi.org/10.3389/fmicb.2023.1188743
26. Ali K, Sajid M, Abu Bakar S et al. (2024) Synthesis of copper oxide (CuO) via coprecipitation method: tailoring structural and optical properties of CuO nanoparticles for optoelectronic device applications. Hybrid Adv 6:100250
27. Balouiri M, Sadiki M, Ibnsouda SK (2016) Methods for in vitro evaluating antimicrobial activity: a review. J Pharm Anal 6:71–79
28. Tacconelli E, Carrara E, Savoldi A et al. (2018) Discovery, research, and development of new antibiotics: the WHO priority list of antibiotic-resistant bacteria and tuberculosis. Lancet Infect Dis 18:318–327
29. Lv J, Li M, Wang X et al. (2025) 4D-printed hydrogel with precise regulation of viability and environment of stem cells for diabetic skin wound healing. Mater Today Bio 35:102366
30. Kayani ZN, Umer M, Riaz S et al. (2015) Characterization of copper oxide nanoparticles fabricated by the sol–gel method. J Electron Mater 44:3704–3709
31. Adeyemi JO, Onwudiwe DC, Oyedeji AO (2022) Biogenic synthesis of CuO, ZnO, and CuO–ZnO nanoparticles using leaf extracts of dovyalis caffra and their biological properties. Molecules 27:3206
32. Pan C, Qian J, Zhao C et al. (2020) Study on the relationship between crosslinking degree and properties of TPP crosslinked chitosan nanoparticles. Carbohydr Polym 241:116349
33. Kumar JA, Krithiga T, Manigandan S, et al (2021) A focus on green synthesis of metal/metal- based oxide nanoparticles: Various mechanisms and applications towards an ecological approach. J Cleaner Production 324 https://doi.org/10.1016/j.jclepro.2021.129198
34. Pasindu V, Munaweera I (2025) Harnessing atomic-scale defect engineering in 2D photocatalysts: synergistic integration of nanocomposite architectures for bandgap tuning and charge transfer optimization. RSC Adv 15:34191–34210
35. Sharma M, Sajwan D, Gouda A et al. (2024) Recent progress in defect-engineered metal oxides for photocatalytic environmental remediation. Photochem Photobio 100:830–896
36. Udoetok IA, Karoyo AH, Mohamed MH et al. (2024) Chitosan biocomposites with variable cross-linking and copper-doping for enhanced phosphate removal. Molecules 29:445
37. Aiedeh KM, Taha MO, Al-Hiari Y et al. (2007) Effect of ionic crosslinking on the drug release properties of chitosan diacetate matrices. J Pharm Sci 96:38–43
38. Zavabeti A, Jannat A, Zhong L et al. (2020) Two-dimensional materials in large areas: synthesis, properties and applications. Nanomicro Lett 12:66
39. Khan F, Shariq M, Asif M et al. (2022) Green nanotechnology: plant-mediated nanoparticle synthesis and application. Nanomaterials 12:673
40. Verma M, Kumar V, Katoch A (2018) Sputtering-based synthesis of CuO nanoparticles and their structural, thermal and optical studies. Mater Sci Semicond Process 76:55–60
41. Thakur S, Shandilya M, Thakur S et al. (2020) Growth mechanism and characterization of CuO nanostructure as a potent Antimicrobial agent. Surf Interfaces 20:100551
42. Shrestha S, Wang B, Dutta P (2020) Nanoparticle processing: understanding and controlling aggregation. Adv Colloid Interface Sci 279:102162
43. Zhang Z, Zhang L, Wang X, et al (2022) Micro/nano-scaled covalent organic frameworks: polymerization, crystallization and self-assembly. ChemNanoMat 8 https://doi.org/10.1002/cnma.202100345
44. Singh H, Desimone MF, Pandya S et al. (2023) Revisiting the green synthesis of nanoparticles: uncovering influences of plant extracts as reducing agents for enhanced synthesis efficiency and its biomedical applications. Int J Nanomed ume 18:4727–4750
45. Gupta D, Boora A, Thakur A et al. (2023) Green and sustainable synthesis of nanomaterials: recent advancements and limitations. Environ Res 231:116316
46. Khoerunnisa F, Nurhayati M, Herlini H et al. (2023) Design and application of chitosan-CuO nanocomposites synthesized via novel hybrid ionic gelation-ultrasonication methods for water disinfection. J Water Process Eng 52:103556
47. Gündeşli MA (2025) Polyphenolic compounds and therapeutic potential of sumac (Rhus coriaria L.): a comprehensive review. Turk J Agric Food Sci Technol 13:3427–3434
48. Arena K, Trovato E, Cacciola F et al. (2022) Phytochemical characterization of Rhus coriaria L. extracts by headspace solid-phase micro extraction gas chromatography, comprehensive two-dimensional liquid chromatography, and antioxidant activity evaluation. Molecules 27:1727

49. Lo Vecchio G, Cicero N, Nava V et al. (2022) Chemical characterization, antibacterial activity, and embryo acute toxicity of Rhus coriaria L. genotype from Sicily (Italy). Foods 11:538
50. Mongy Y, Shalaby T (2024) Green synthesis of zinc oxide nanoparticles using Rhus coriaria extract and their anticancer activity against triple-negative breast cancer cells. Sci Rep 14:13470
51. Mamand DM, Muhammad DS, Muheddin DQ et al. (2025) Optical band gap modulation in functionalized chitosan biopolymer hybrids using absorption and derivative spectrum fitting methods: a spectroscopic analysis. Sci Rep 15:3162
52. Nzilu DM, Madivoli ES, Makhanu DS et al. (2023) Green synthesis of copper oxide nanoparticles and its efficiency in degradation of rifampicin antibiotic. Sci Rep 13:14030
53. Karu E, Magaji B, Atiko R et al. (2024) Green synthesis, spectroscopic analysis, and stabilisation energies of copper and manganese oxide nanoparticles from aqueous Mentha piperita leaf extract. Dutse J Pure Appl Sci 10:161–172
54. Tshireletso P, Ateba CN, Fayemi OE (2021) Spectroscopic and antibacterial properties of CuONPs from orange, lemon and tangerine peel extracts: potential for combating bacterial resistance. Molecules 26:586
55. P K DrI, Mruthunjaya K, Hanagodimath SM et al. (2025) Chemical and green synthesis of CuO nanoparticles using carica papaya leaf extract: structural and optical properties. J Condens Matter 2:12–19
56. Singh D, Jain D, Rajpurohit D, et al (2023) Bacteria-assisted green synthesis of copper oxide nanoparticles and their potential applications as antimicrobial agents and plant growth stimulants. Front Chem 11 https://doi.org/10.3389/fchem.2023.1154128
57. Gebrie HT, Assege MA, Meshesha DS et al. (2025) Biosynthesis and characterization of copper oxide nanoparticles from Plumbago zeylanica leaf extract for antibacterial and antioxidant activities. Sci Rep 15:30656
58. Umoren PS, Kavaz D, Nzila A et al. (2022) Biogenic synthesis and characterization of chitosan-Cuo nanocomposite and evaluation of antibacterial activity against gram-positive and -negative Bacteria. Polymers 14:1832
59. Sathiyavimal S, Vasantharaj S, Kaliannan T et al. (2020) Eco-biocompatibility of chitosan- coated biosynthesized copper oxide nanocomposite for enhanced industrial (Azo) dye removal from aqueous solution and antibacterial properties. Carbohydr Polym 241:116243
60. Rakshit S, Mondal KG, Jana PC et al. (2023) Structural and optical properties of chemically synthesized copper oxide nanoparticles and their photocatalytic application. J Mater Sci Mater Electron 34:2141
61. Rakshit S, Maji D, Mondal KG et al. (2024) Structural, optical and magnetic properties of chemically grown copper oxide nanoparticles: an insight into anticancer activities. Mater Chem Phys 325:129794
62. Nouren S, Bibi I, Kausar A et al. (2024) Green synthesis of CuO nanoparticles using Jasmin sambac extract: conditions optimization and photocatalytic degradation of Methylene Blue dye. J King Saud Univ Sci 36:103089
63. Moroda MD, Leta Deressa T, Tiwikrama AH et al. (2025) Green synthesis of copper oxide nanoparticles using Rosmarinus officinalis leaf extract and evaluation of its antimicrobial activity. Materials 7:100337
64. Malakhovska TO, Pogodin AI, Filep MJ et al. (2024) Structure and optical characterization of chitosan-chitin/Ag nanocomposite thin films. Semiconduct Phys Quantum Electron Optoelectron 27:040–053
65. Omar A, Badry R, Hegazy MA et al. (2022) Enhancing the optical properties of chitosan, carboxymethyl cellulose, sodium alginate modified with nano metal oxide and graphene oxide. Opt Quantum Electron 54:806
66. Selvanathan V, Aminuzzaman M, Tey L-H et al. (2021) Muntingia calabura leaves mediated green synthesis of CuO nanorods: exploiting phytochemicals for unique morphology. Materials 14:6379
67. Aouadi A, Hamada Saud D, Rebiai A et al. (2024) Introducing the antibacterial and photocatalytic degradation potentials of biosynthesized chitosan, chitosan–ZnO, and chitosan–ZnO/PVP nanoparticles. Sci Rep 14:14753
68. Guo Y, Dai M, Zhu Z et al. (2019) Chitosan modified Cu2O nanoparticles with high catalytic activity for p-nitrophenol reduction. Appl Surf Sci 480:601–610
69. El-Morsy MA, Awwad NS, Ali HE et al. (2022) Optical, thermal and dielectric properties of Copper Oxide (CuO)/ chitosan (CS)/ Polyethylene oxide (PEO) blends. J Polym Res 29:177
70. Alhusaiki Alghamdi HM (2022) Structural, morphological, optical, and electrical characteristics of polyethylene oxide/ chitosan-copper oxide nanoparticles for optoelectronic applications. Opt Mater 134:113101
71. Katubi KM, Jabeen A, Alrowaili ZA et al. (2025) The correlation of bandgap with the crystallite size using the quantum confinement effect for wastewater treatment. Desalin Water Treat 322:101115
72. Siddiqi KS, Husen A (2020) Current status of plant metabolite-based fabrication of copper/copper oxide nanoparticles and their applications: a review. Biomater Res 24 https://doi.org/10.1186/s40824-020-00188-1
73. Mirbagheri VS, Alishahi A, Ahmadian G et al. (2024) Toward understanding the antibacterial mechanism of chitosan: experimental approach and in silico analysis. Food Hydrocoll 147:109382
74. Rashki S, Asgarpour K, Tarrahimofrad H et al. (2021) Chitosan-based nanoparticles against bacterial infections. Carbohydr Polym 251:117108
75. Laanoja J, Sihtmäe M, Vihodceva S et al. (2024) Synthesis and synergistic antibacterial efficiency of chitosan-copper oxide nanocomposites. Heliyon 10:e35588
76. Wang Y-L, Lee Y-H, Chou C-L et al. (2024) Oxidative stress and potential effects of metal nanoparticles: a review of biocompatibility and toxicity concerns. Environ Pollut 346:123617
77. Kessler A, Hedberg J, Blomberg E et al. (2022) Reactive oxygen species formed by metal and metal oxide nanoparticles in physiological media—a review of reactions of importance to nanotoxicity and proposal for categorization. Nanomaterials 12:1922
78. Khort A, Brookman-Amissah M, Hedberg J et al. (2022) Influence of natural organic matter on the transformation of metal and metal oxide nanoparticles and their ecotoxic potency in vitro. NanoImpact 25:100386
79. Sajjad H, Sajjad A, Haya RT et al. (2023) Copper oxide nanoparticles: In vitro and in vivo toxicity, mechanisms of action and factors influencing their toxicology. Comp Biochem Physiol Part C Toxicol Pharmacol 271:109682
80. Harugade A, Sherje AP, Pethe A (2023) Chitosan: a review on properties, biological activities and recent progress in biomedical applications. React Funct Polym 191:105634
81. Zoe LH, David SR, Rajabalaya R (2023) Chitosan nanoparticle toxicity: a comprehensive literature review of in vivo and in vitro assessments for medical applications. Toxicol Rep 11:83–106
82. Canbolat F, Demir N, Yayıntas OT et al. (2024) Chitosan nanoparticles loaded with quercetin and valproic acid: a novel approach for enhancing antioxidant activity against oxidative stress in the SH-SY5Y human neuroblastoma cell line. Biomedicines 12:287
83. Limprasart W, Sangkaworn J, Paosopa S et al. (2025) Cu(II) supported on crosslinked chitosan-cellulose beads as efficient and recyclable catalysts for oxidative self-coupling of amines to imines. Carbohydr Polym Technol Appl 9:100660

84. Wang Z, Li Y, Wang C et al. (2026) Disrupting intracellular redox homeostasis through copper-driven dual cell death to induce anti-tumor immunotherapy. Biomaterials 324:123523
85. Cheng Y, Zhang H, Qu X (2021) Electronic band-engineered nanomaterials for biosafety and biomedical application. Acc Mater Res 2:764–779
86. Tsakiroglou P, VandenAkker NE, Del Bo' C et al. (2019) Role of berry anthocyanins and phenolic acids on cell migration and angiogenesis: an updated overview. Nutrients 11:1075
87. Shang S, Zhuang K, Chen J et al. (2024) A bioactive composite hydrogel dressing that promotes healing of both acute and chronic diabetic skin wounds. Bioact Mater 34:298–310